

Intrinsic shapes of Brightest Cluster Galaxies

STEFANO DE NICOLA,^{1,*} ROBERTO P. SAGLIA,^{1,2} JENS THOMAS,^{1,2} CLAUDIA PULSONI,¹ MATTHIAS KLUGE,^{2,1}
RALF BENDER,^{2,1} LUCAS M. VALENZUELA,² AND RHEA-SILVIA REMUS²

¹*Max-Planck Institute for Extraterrestrial Physics, Giessenbachstrasse 1, D-85748, Garching (Germany)*

²*Universitäts-Sternwarte München, Scheinerstrasse 1, D-81679, Munich, Germany*

ABSTRACT

We discuss the statistical distribution of galaxy shapes and viewing angles under the assumption of triaxiality by deprojecting observed Surface Brightness (SB) profiles of 56 Brightest Cluster Galaxies coming from a recently published large deep-photometry sample. For the first time, we address this issue by directly measuring axis ratio profiles without limiting ourselves to a statistical analysis of average ellipticities. We show that these objects are strongly triaxial, with triaxiality parameters $0.39 \leq T \leq 0.72$, have on average axis ratios $\langle p(r) \rangle = 0.84$ and $\langle q(r) \rangle = 0.68$, and are more spherical in the central regions but flatten out at large radii. Measured shapes in the outskirts agree well with the shapes found for simulated massive galaxies and their dark matter halos from both the IllustrisTNG and the Magneticum simulations, possibly probing the nature of dark matter. In contrast, both simulations fail to reproduce the observed inner regions of BCGs, producing too flattened objects.

Keywords: celestial mechanics, stellar dynamics – galaxies: elliptical and lenticular, cD – galaxies: kinematics and dynamics – galaxies: structure

1. INTRODUCTION

Massive elliptical galaxies show, when observed projected on the plane of the sky, smooth elliptical contours with mild boxy deviations (e.g. Bender & Möllenhoff 1987), small twists (typically $\lesssim 10^\circ$) and increasing ellipticity (ε) profiles towards outer radii (Goullaud et al. 2018). The average projected flattening is $\langle q' \rangle \sim 0.8$ (Tremblay & Merritt 1996; Weijmans et al. 2014; Chen et al. 2016; Ene et al. 2018), with $q' \equiv 1 - \varepsilon$. The presence of isophote twists, together with other factors such as the statistical distribution of ellipticity profiles provides evidence for the triaxiality of these objects (Illingworth & King 1977; Bertola & Galletta 1978; Vincent & Ryden 2005).

Various works in the last 25 years have studied the average statistical distribution of intrinsic shapes for large galaxy samples at different redshifts z (Tremblay & Merritt 1996; Vincent & Ryden 2005; Weijmans et al. 2014; Chang et al. 2013; Chen et al. 2016; Ene et al. 2018; Li et al. 2018a). Deprojecting these distributions (e.g. Tremblay & Merritt 1996) allows to recover the *average* or *typical* intrinsic shape of the galaxies. These studies find that most massive objects are indeed triaxial, with

a mean triaxiality parameter $T = (1 - p^2) / (1 - q^2)$ (Franx et al. 1991) in the range $[0.4, 0.8]$ (Vincent & Ryden 2005), where $p \equiv b/a$, $q \equiv c/a$, and $a \geq b \geq c$ are the lengths of the three principal axes of the density ellipsoid. However, no study has yet attempted to *directly measure radially resolved intrinsic shapes of individual galaxies in large samples*.

In a recent paper, de Nicola et al. (2020) have presented a triaxial deprojection routine that fits the intrinsic shape of ellipsoidal galaxies and allows to constrain the viewing angles under which an object is seen by photometric data alone. This can be refined further in combination with the dynamical modeling of appropriate stellar kinematics (de Nicola et al., in prep.), since the number of deprojections which need to be tested is drastically reduced, allowing the study of large samples of galaxies.

An interesting group of massive galaxies consists of the so-called Brightest Cluster Galaxies (BCGs). According to Kluge et al. (2020), a BCG is defined as the closest galaxy to the geometrical and the kinematical centre of a given galaxy cluster, although not necessarily the most luminous galaxy of the cluster itself. Lying deep in the potential well of the cluster, these giant ellipticals are able to increase their mass through processes such as galaxy mergers (Contini et al. 2018), cannibalism or

* denicola@mpe.mpg.de

tidal stripping (Mo et al. 2008). In a recent paper by Kluge et al. (2020), a sample of 170 BCGs was analyzed in great detail using extremely deep photometric observations, revealing that BCGs follow different scaling relations with respect to ordinary ETGs. BCGs are also interesting because their outer parts have probably grown predominantly by collision-less accretion and, hence, in a manner similar to the proposed growth of (collision-less) dark-matter halos.

The first goal of this paper is to constrain the intrinsic shapes and viewing angles of a representative subsample (56 objects) of this BCG catalogue with the deprojection method of de Nicola et al. (2020). Then, our second goal is to compare the recovered shapes to the ones of simulated massive galaxies and their dark matter halos. For this purpose we consider the IllustrisTNG (Nelson et al. 2018; Springel et al. 2018; Marinacci et al. 2018; Naiman et al. 2018; Pillepich et al. 2018) and Magneticum pathfinder (Hirschmann et al. 2014; Teklu et al. 2015¹) simulations. These cosmological (magneto)-hydrodynamical model the formation and evolution of galaxies in a Λ CDM Universe including recipes for star formation and evolution, chemical enrichment of the inter-stellar medium, gas cooling and heating, black hole and supernova feedback. These simulations produce galaxy populations with properties in reasonable agreement with observations (Remus et al. 2017; Teklu et al. 2017; Genel et al. 2018; van de Sande et al. 2019; Rodriguez-Gomez et al. 2019; Pulsoni et al. 2020; Remus & Forbes 2021).

The paper is structured as follows. Section 2 describes the galaxy sample used in this work. In Section 3 we explain the deprojection procedure. In Section 4 we present the results on the statistics of triaxial shapes and compare our findings with the TNG and Magneticum simulations. Finally, we draw our conclusions in Section 5. Throughout the paper we assume a flat cosmology with $H_0 = 69.6 \text{ km s}^{-1} \text{ Mpc}^{-1}$ and $\Omega_m = 0.286$.

2. THE SAMPLE

The BCGs studied in this work come from a recently published sample (Tab. 1 of Kluge et al. 2020). Each BCG was observed in the g' band with the 2m Fraunhofer telescope at the Wendelstein Observatory (see Kluge et al. 2020 for technical details). The photometry has exactly the requirements needed for the present work, being extremely deep (down to $m_{g'} \sim 30$ mag) and reaching very large radii (typically well beyond 100 kpc). From the complete sample, we extract those objects for which supplementary F606W HST photometry

(typical resolution $\sim 0.15''$) is available, excluding galaxies that are overall unrelaxed (see below). To combine these high-resolution data with those coming from Wendelstein observations, we first select the radii where we have data from both observation sets that are not affected by seeing (typically from 5 to 15 arcsec from the center), then we interpolate HST photometry at Wendelstein radii. Finally, we convert the HST data to the g' band, by determining the sky level and the scaling factor that minimize the differences between the two photometric sets. We combine the two sets by taking the HST values in the inner 10-15 arcsec, and the Wendelstein values at larger radii. In this way we have photometric data with both very high resolution in the center and also extending out to ~ 100 kpc for the majority of the objects². We complement this list with further 8 BCGs which we recently observed both in the H and/or Ks bands at the 8.4m Large Binocular Telescope (LBT) using Adaptive Optics, with typical resolution of $\sim 0.4''$. We combine the LBT photometry with the Wendelstein one using the same approach described above. In App. A we show a comparison of the deprojection of two galaxies with and without high-resolution photometry to explore possible photometric effects, showing that they are small. Without high resolution data, the deprojections cannot probe the central regions of the galaxies, but reliable profiles are derived at larger radii.

This allows us to add 16 more BCGs with only Wendelstein data, for a total of 56 galaxies. The average isophotal flattening $\langle q' \rangle$ is ~ 0.77 , although almost every BCG becomes very flat ($q' \lesssim 0.4$) at large radii. In App. B we show the ε and PA profiles for every BCG of the sample.

Since BCGs often show signs of interactions with other neighbor galaxies of the cluster or AGN activity in the central regions (Kluge et al. 2020), and given that our triaxial code works under the assumption of (smooth) "deformed ellipsoids" (see eq. 29 of de Nicola et al. 2020), we omit the innermost/outermost isophotes from the deprojection when we find signs of incomplete relaxation (for example, in the form of bumpy ε or PA profiles). This happens in the very center (e.g. AGNs, ongoing accretion) or in the very outer parts (where dynamical time scales are large). Notes on individual galaxies can be found in App. D. Since we are interested in comparing our findings with simulations at large radii, we try, when possible, to extend the deprojection up to

² As shown by Kluge et al. (2020), at larger radii (typically as SB approaches 27-28 mag arcsec⁻²) isophotal shape profiles become too noisy to be estimated reliably.

¹ www.magneticum.org

Variable	Intervals	R_N
	≤ 0.02	1.0
z	$[0.02, 0.05]$	~ 0.5
	≥ 0.05	~ 0.15
R_e	≥ 50	~ 0.25
M_{tot}	$[-22, -26]$	~ 0.25

Table 1. The ratio R_N of the number of galaxies in our sub-sample N_{sub} for a given interval to the number of galaxies in the full sample N_{full} for three variables of interest. Our sub-sample is biased towards low-redshift galaxies, while no significant bias in magnitude and effective radii is found.

$2 - 4R_e$, with the values for half-light radii R_e taken from Tab. 4 of Kluge et al. (2020).

2.1. Selection effects

The full sample of Kluge et al. (2020) is drawn from the Abell–Corwin–Olowin catalog (ACO, Abell et al. 1989) by adopting redshift and volume-limiting constraints. It contains BCGs with redshift $z \lesssim 0.08$ (with 15 outliers) and has a slight Malmquist bias (see their Figure 3). However, a comparison of this sample with other large samples, also drawn from ACO, shows that they have about 80-90% of the objects in common.

In order to check the completeness of our sub-sample, we define R_N as the ratio of the number of galaxies in our sub-sample N_{sub} to the number of galaxies in the full sample N_{full} . We become progressively incomplete at larger redshifts: at $z \leq 0.04$, we have $0.5 \leq R_N \leq 1.0$, but at larger redshifts R_N is ≤ 0.2 . Moreover, Fig. 1, left panel, shows that the mean redshift and redshift range covered by our subsample are smaller than the ones of the parent sample. This is expected, since both HST- and LBT-observed galaxies are at lower redshift than the average, and we picked them up to perform dynamical modeling.

We do not find significant selection effects when considering the size (Fig. 1, middle panel) or the total absolute magnitude of the galaxies M_{tot} , (Fig. 1, right panel). The results are summarised in Tab. 1.

3. DEPROJECTION PROCEDURE

In this section we describe the deprojection parameters used for the BCGs. An extensive description of the deprojection routine itself is given by de Nicola et al. (2020). In short, given the observed surface luminosity $I_{\text{obs}} = L/pc^2$ onto a polar elliptical grid, the code searches for the three-dimensional luminosity

density ρ , placed onto an ellipsoidal grid, whose corresponding projected surface luminosity I_{fit} minimizes $\text{RMS} = \sqrt{\langle (\ln(I_{\text{obs}}/I_{\text{fit}}))^2 \rangle}$. The algorithm works under the assumption that a galaxy can be described by what we call a “deformed ellipsoid”, namely an ellipsoid whose radius is given by

$$m^{2-\xi(x)} = x^{2-\xi(x)} + \left[\frac{y}{p(x)} \right]^{2-\xi(x)} + \left[\frac{z}{q(x)} \right]^{2-\xi(x)} \quad (1)$$

where the exponent ξ can be used to generate disk ($\xi=0$) or boxy ($\xi>0$) bias. The three one-dimensional functions $p(x)$, $q(x)$, and $\xi(x)$, along with the density on the x-axis $\rho_x(x)$, specify ρ at each point of the grid. Finally, the code uses a one-dimensional radial smoothing on $p(x)$, $q(x)$, $\xi(x)$ and $\rho_x(x)$ to penalize against unsmooth solutions.

3.1. Choice of parameters

Table 2 highlights for each BCG the parameters used for the deprojections. In the following we will give a detailed explanation of these parameters.

- *Grid sampling.* It is important to place both the observed I_{obs} and deprojected ρ on grids large enough to reproduce photometric information properly, but at the same time a very large grid would slow down the code significantly. Therefore, we start by interpolating the SB onto a finely sampled grid, and then gradually reduce both the number of radial ($n_{r'}$) and angular points ($n_{\theta'}$) as long as the comparison with the observations remains acceptable, that is, an error below 1% for every photometric variable (SB, ε , PA, a_4 , a_6). Then, we set the number of radial points of the ρ -grid $n_r = n_{r'} + 20$, while the numbers of angular points n_θ and n_ϕ are typically the same as ($n_{\theta'}$) or slightly larger.
- *Grid extension in radius.* The innermost radii are the same for both grids, namely the semiminor axis of the innermost isophote. These have to be estimated for every BCG by taking into account the spatial resolution of the observations and by checking whether the galaxy shows central activity. In this last case, central regions are omitted. The outermost radii for the SB grid are estimated by making use of our software for isophotal fitting (Bender & Möllenhoff 1987). We typically stop when the isophotal shape profiles become noisy and have to be set to a constant values (typically at SB ~ 27 -28 mag asec^{-2}). The largest radii

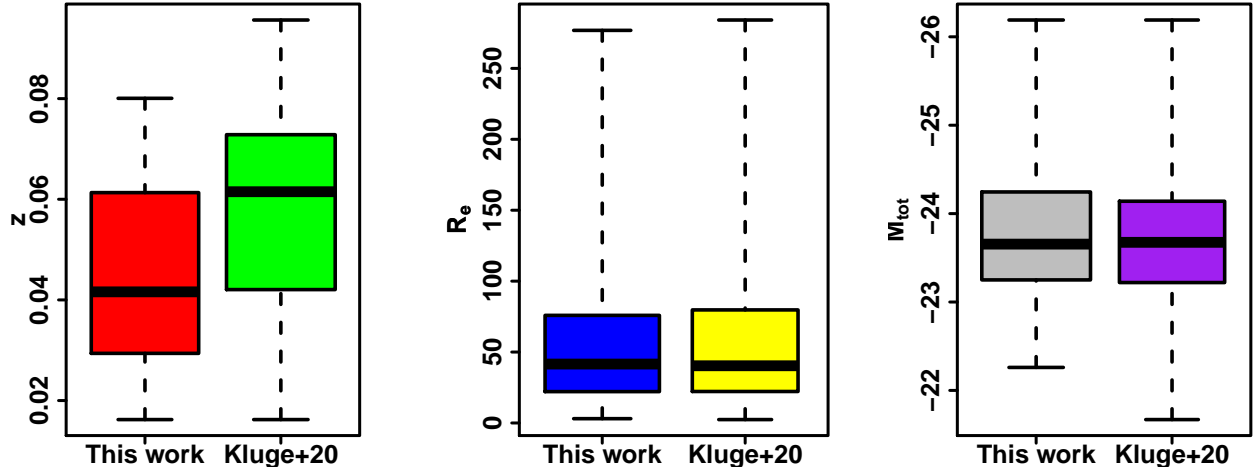


Figure 1. Boxplots showing redshifts (left panel), effective radii (central panel) and g' magnitudes (right panel) for Kluge et al. (2020)’s sample and our sub-sample. Our sub-sample is biased towards galaxies at lower redshift and also slightly towards galaxies with high R_e . Boxes are drawn from the first to the third quartiles, with the horizontal line in the middle of the boxes denoting the median. Whiskers span across the whole data range.

of the ρ -grid are then a few times those of the corresponding SB grid.

- *Grid flattenings.* The flattening of the SB grid can easily be estimated by considering the isophote PAs. For example, if a galaxy shows isophote structures with the major axes aligned along the vertical axis on the plane of the sky y' , it makes sense to use an elliptical polar grid flattened in the x' -direction, even with a 15-20° twist. As far as it concerns ρ , we first assume a spherical grid, then we re-project the galaxies at the best-fit inclination(s) using the recovered $\langle p(r) \rangle$ and $\langle q(r) \rangle$ as flattenings.
- *Smoothing.* As shown in de Nicola et al. (in prep.) we can recover the true *intrinsic* density of a triaxial N -body simulation with an RMS of $\sim 10\%$. Since it is not entirely clear how to estimate the smoothing a priori, we take the four λ -values $[\lambda_\rho, \lambda_p, \lambda_q, \lambda_\xi]$ (cfr. eq. 30 of de Nicola et al. 2020) used with the simulation divided by a factor of 2, to take into account that our data are less noisy than the N -body simulation (the smoothing scales as λ^{-2}). Since the smoothing value affects the RMS one gets at the end (the higher the smoothing, the higher the RMS), we verified that for the best galaxies the RMS was comparable to the one we got for the simulation. The values we chose are $[0.6, 0.03, 0.03, 0.3]$. A more rigorous implementation would be the minimization of the

Akaike Information Criterion (AIC, Akaike 1974), as shown by Lipka & Thomas (2021); Thomas & Lipka (2022). We defer this to a forthcoming paper.

- *Constraints on p, q .* Our code allows the possibility of deprojecting by imposing constraints on p, q . Since the code has shown excellent results in terms of recovering the right profiles, we only impose $p, q \geq 0.2$, to prevent too flat solutions which may give problems to the fit.

3.2. Viewing angles

Deprojections yield in general a non-unique solution (Gerhard 1996; van den Bosch 1997; de Nicola et al. 2020), unless one uses constraints about the galaxy shape. We impose the resulting deprojection to consist of a series of concentric perfect ellipsoids, i.e. setting $\xi(r) = 0$ at all radii³, and without imposing biasing towards certain p, q profiles. Further parameters to be considered are the three viewing angles (θ, ϕ, ψ) required to identify the orientation in space of a triaxial galaxy. The first two give the orientation of the line-of-sight (LOS) in space, whereas the third one is a rotation about the LOS itself. If one could measure these angles, then the intrinsic axis ratios of the ellipsoid could be cal-

³ This assumption is justified by the fact that for the BCGs the deviations from elliptical shapes are small, i.e. $|a_4/a| < 5\%$ in the deprojected regions.

Galaxy	arcsec/kpc	r_{\min}	r_{\max}	I_{obs} grid	ρ grid	Photometry
2MASXJ0753	1.17	2.13	128.1	40×15	$60 \times 16 \times 16$	L + W
2MASXJ0900	1.426	2.35	104.2	50×15	$70 \times 15 \times 15$	W
2MASXJ1358	1.225	1.98	74.04	40×10	$60 \times 11 \times 11$	W
IC613	0.653	0.0940	116.1	50×10	$70 \times 11 \times 11$	H + W
IC664	0.679	0.0984	76.0	40×10	$60 \times 11 \times 11$	H + W
IC1101	1.48	1.06	70.2	40×12	$60 \times 13 \times 13$	H + W
IC1565	0.765	0.101	243.2	40×10	$60 \times 11 \times 11$	H + W
IC1634	1.336	1.58	156.8	50×10	$70 \times 11 \times 11$	W
IC1695	0.987	0.150	149.1	40×10	$60 \times 11 \times 11$	H + W
IC1733	0.714	0.528	33.8	30×12	$50 \times 13 \times 13$	W
IC2378	0.990	0.762	58.5	40×10	$60 \times 11 \times 11$	H + W
IC5338	1.10	4.91	178.3	40×10	$60 \times 11 \times 11$	H + W
LEDA1518	1.248	4.16	117.1	40×10	$60 \times 11 \times 11$	W
LEDA2098	1.467	2.82	127.3	40×10	$60 \times 11 \times 11$	W
MCG+01-60	1.16	0.622	38.4	30×12	$50 \times 13 \times 13$	W
MCG-02-02	1.083	3.44	173.7	40×10	$60 \times 11 \times 11$	W
MCG+02-04	0.869	0.213	184.3	50×12	$70 \times 13 \times 13$	H + W
MCG+02-27	0.653	0.114	103.4	40×10	$60 \times 11 \times 11$	H + W
MCG+02-58	1.52	1.69	100.1	40×10	$60 \times 11 \times 11$	H + W
MCG+03-04	1.375	2.76	66.34	40×10	$60 \times 11 \times 11$	W
MCG+03-38	0.886	0.165	87.6	40×10	$60 \times 11 \times 11$	H + W
MCG+04-28	2.53	1.15	299.7	40×12	$60 \times 13 \times 13$	H + W
MCG+05-32	1.44	1.19	312.9	40×10	$60 \times 11 \times 11$	H + W
MCG+05-33	1.23	2.64	67.1	40×10	$60 \times 11 \times 11$	H + W
MCG+09-13	1.362	3.78	103.1	40×10	$60 \times 11 \times 11$	W
MCG+09-20	1.296	2.49	133.4	40×10	$60 \times 11 \times 11$	W
NGC708	0.332	0.0551	61.2	40×15	$60 \times 15 \times 15$	H + W
NGC910	0.354	0.611	70.4	40×10	$60 \times 11 \times 11$	H + W
NGC1128	0.486	0.0895	31.7	40×10	$60 \times 11 \times 11$	H + W
NGC1129	0.361	0.160	98.0	60×12	$80 \times 12 \times 12$	H + W
NGC1275	0.359	0.739	81.9	40×10	$60 \times 11 \times 11$	W
NGC2329	0.396	0.534	43.3	50×12	$70 \times 13 \times 13$	H + W
NGC2804	0.559	1.58	35.6	40×10	$60 \times 11 \times 11$	W
NGC3550	0.703	0.505	99.9	40×12	$60 \times 13 \times 13$	L + W
NGC3551	0.640	0.382	33.4	30×12	$50 \times 13 \times 13$	W
NGC4104	0.577	0.970	60.2	40×12	$60 \times 13 \times 13$	L + W
NGC4874	0.469	0.0905	98.6	50×10	$70 \times 11 \times 11$	H + W
NGC6166	0.622	0.718	94.9	40×10	$60 \times 11 \times 11$	H + W
NGC6173	0.592	0.0613	109.2	40×10	$60 \times 11 \times 11$	H + W
NGC6338	0.552	0.334	132.4	50×10	$70 \times 11 \times 11$	H + W
NGC7647	0.818	0.323	97.5	50×10	$70 \times 11 \times 11$	H + W
NGC7649	0.835	0.659	94.1	40×10	$60 \times 11 \times 11$	H + W
NGC7720	0.611	0.720	153.1	40×10	$60 \times 11 \times 11$	H + W
NGC7768	0.545	0.307	102.3	40×10	$60 \times 11 \times 11$	H + W
SDSSJ0837	2.67	1.66	118.0	40×20	$60 \times 20 \times 20$	L + W
UGC716	1.19	0.832	175.7	40×10	$60 \times 11 \times 11$	L + W
UGC727	1.135	1.89	114.4	40×10	$60 \times 11 \times 11$	W
UGC1191	1.21	0.638	124.5	40×20	$60 \times 20 \times 20$	L + W
UGC2232	0.958	0.152	95.3	40×10	$60 \times 11 \times 11$	H + W
UGC2413	0.690	0.379	113.4	50×10	$70 \times 11 \times 11$	H + W
UGC4289	0.587	0.587	50.1	40×10	$60 \times 11 \times 11$	H + W
UGC6394	0.847	1.99	97.2	40×10	$60 \times 11 \times 11$	W
UGC9799	0.691	4.13	97.7	40×10	$60 \times 11 \times 11$	H + W
UGC10143	0.708	0.584	110.6	50×10	$70 \times 11 \times 11$	H + W
UGC10726	1.15	0.704	189.8	60×12	$80 \times 12 \times 12$	L + W
VV161C	0.354	0.401	181.8	40×10	$60 \times 11 \times 11$	L + W

Table 2. *Col. 1:* Galaxy name. *Col. 2:* arcsec/kpc conversion factor. *Cols. 3-4:* Smallest and largest isophotal radii, in kpc. *Cols. 5-6:* I_{obs} and ρ -grid dimensions. *Col. 7:* The available photometry (W: Wendelstein, H: HST, L: LBT).

culated analytically. Since this is not usually the case, we need to sample a grid of viewing angles and deproject every BCG trying out every set of viewing angles. The assumption of triaxiality, i.e. the galaxy has an 8-fold symmetry, allows us to sample the two viewing angles (θ, ϕ) in $[0, \pi/2]$, while ψ needs to be sampled in $[0, \pi]$. We sample each angle in 10° step, which gives us a total of 1800 inclinations to test for each BCG. As shown by de Nicola et al. (2020), although the viewing angle estimate through deprojections is not always perfect, the list of "good" solutions (see below) *always* includes the correct viewing angles.

In the same paper, the authors show that sampling one octant does not guarantee the "canonical" $1 \geq p \geq q$ order relationship (cfr. their Table 2). However, for a given deprojected density at a given set of viewing angles for which this does not happen, *it is always possible to find another set of viewing angles for which the deprojection is equivalent but with $1 \geq p \geq q$* , possibly in the octant with $\phi \in [\pi/2, \pi]$. In this case, if the density happens to be a "good" one in terms of the RMS (see below), we re-perform the deprojection for this new set of viewing angles such that the inequality $1 \geq p \geq q$ holds.

In order to find the "good" deprojections, we isolate for every galaxy g all viewing angles for which the deprojection has $\mathcal{R}_g \leq \delta \times \mathcal{R}_{\min,g}$, where $\mathcal{R}_g \equiv \text{RMS}_g$ is the RMS and $\mathcal{R}_{\min,g}$ is the smallest RMS that we find among all viewing angles that we sampled for galaxy g . The factor δ determines how stringent the cut-off is. In another work aiming at modeling an N -body simulation (de Nicola et al., in prep.), we adopt values in the range $\delta = 1.2 - 1.5$ studying the impact of the choice of this value on the number of plausible deprojections. Here, we try to be conservative adopting $\delta = 1.5$. The resulting light densities are those that we use to derive the results shown in Sec. 4.2.

Finally, we note that there may still be a degeneracy between the model and orientation parameters, but this is small and will not be taken into account throughout the remainder of the paper. In App. A we examine the case of NGC7647, and derive profiles for the best-fit viewing angles, stopping the deprojection when the RMS reaches 1.5 RMS_{\min} (which is the best value achievable). These p & q profiles are well within the range obtained by considering all possible viewing angles.

4. RESULTS

Using the cut-off described in Sec. 3.2 we are able to reduce the number of inclinations from the initial value of 1800 by at least a factor of 3. The typical RMS values

for the best-fit solutions are 0.01 to 0.03. The results are summarized in Tab. 3.

4.1. Reliability of the deprojections

As a first step we verify that our deprojections do reproduce the average photometry of the sample. First, we calculate for every galaxy the mean ε and the twist, defined as $\Delta\text{PA} = \max(\text{PA}) - \min(\text{PA})$, both for the observed and the recovered photometry. Moreover, we reproject the best-fit densities ρ_g for every galaxy g at three different random viewing angles, computing the same averages as above. This is a good test to statistically verify that the recovered intrinsic shapes are compatible with the observed shape distribution. In Fig. 2 we show the histograms for ε (top row) and the twist (bottom row). A Kolmogoroff-Smirnov (KS, Kolmogoroff 1933; Smirnov 1939) test returns p-values above the canonical 5% threshold⁴ for both the ε and PA distributions, with this being valid for both the best-fit angles and the reprojections at random viewing angles. This confirms that the recovered photometric variables are statistically representative of the BCG sample.

A second step, we check the distribution of the two best-fit angles $\langle(\theta, \phi)\rangle$, which specify the LOS position on the plane of the sky. In the upper panels of Fig. 3 we plot the two octants with the best-fit $\langle(\theta, \phi)\rangle$ onto them. We see that there is a lack of solutions near the principal axes, but this is only given by the fact that we are plotting *only the best-fit solution for each galaxy*. This clearly disfavours such viewing angles, because isophotal twists cannot occur along the principal axes of an ellipsoidal body. Hence, fits along an assumed LOS that coincides with one of the principal axes will deliver larger values of the RMS. In the bottom panel of Fig. 3 we show the entire distribution of deprojections over the two octants for the galaxy NGC708. Solutions on the principal axes are not excluded but lead on average to less good fits. Other examples are provided in the notes in App. D.

4.2. Distribution of intrinsic axis ratios

We now present the *measured* shapes of the BCGs. Our deprojection algorithm *directly* yields the intrinsic axis ratios $p(r)$ and $q(r)$ as a function of the distance from the galaxy center. From these profiles, we compute the triaxiality parameter as a function of the radius $T(r)$. The profiles which we obtain by averaging over all good deprojections are shown in Fig. 12. The left and central panels of Fig. 4 show the histograms of the average over all radial bins and over all accept-

⁴ This corresponds to values in the range 0.194-0.243 for the KS statistics D_n .

Galaxy	$10^2 \times \text{RMS}_{\text{best}}$	Good Deprojections	best-fit angles	$\langle p \rangle$	$\langle q \rangle$	Δ_p	Δ_q
2MASXJ0753	5.1	96	(26,27,37) $^\circ$	0.804	0.661	0.048	0.054
2MASXJ0900	2.2	114	(54,37,122) $^\circ$	0.902	0.769	0.053	0.047
2MASXJ1358	5.0	62	(50,40,60) $^\circ$	0.806	0.568	0.123	0.111
IC613	2.6	250	(70,50,90) $^\circ$	0.879	0.782	0.047	0.040
IC664	3.2	204	(60,40,145) $^\circ$	0.871	0.704	0.080	0.073
IC1101	3.0	28	(50,80,160) $^\circ$	0.798	0.644	0.076	0.075
IC1565	2.4	312	(60,28,167) $^\circ$	0.833	0.697	0.041	0.041
IC1634	2.8	378	(60,40,110) $^\circ$	0.897	0.760	0.050	0.058
IC1695	2.9	376	(50,40,80) $^\circ$	0.854	0.712	0.061	0.057
IC1733	0.73	380	(53,16,165) $^\circ$	0.815	0.695	0.108	0.116
IC2378	1.6	118	(70,100,150) $^\circ$	0.841	0.708	0.082	0.065
IC5338	3.2	58	(60,40,160) $^\circ$	0.824	0.615	0.082	0.073
LEDA1518	4.1	146	(60,60,120) $^\circ$	0.876	0.711	0.091	0.113
LEDA2098	2.3	64	(60,30,60) $^\circ$	0.858	0.716	0.067	0.066
MCG+01-60	0.81	330	(36,34,110) $^\circ$	0.909	0.824	0.084	0.122
MCG-02-02	2.2	94	(60,50,15) $^\circ$	0.786	0.560	0.084	0.081
MCG+02-04	2.6	128	(70,130,90) $^\circ$	0.876	0.747	0.033	0.033
MCG+02-27	3.0	184	(60,132,3) $^\circ$	0.799	0.567	0.076	0.062
MCG+02-58	4.2	96	(60,100,130) $^\circ$	0.763	0.632	0.082	0.101
MCG+03-04	2.3	114	(60,150,90) $^\circ$	0.963	0.900	0.049	0.044
MCG+03-38	2.1	222	(60,140,145) $^\circ$	0.903	0.813	0.075	0.060
MCG+04-28	12.7	144	(80,120,10) $^\circ$	0.877	0.763	0.107	0.127
MCG+05-32	3.0	142	(56,143,3) $^\circ$	0.841	0.639	0.056	0.062
MCG+05-33	2.6	112	(80,90,165) $^\circ$	0.889	0.793	0.067	0.069
MCG+09-13	2.8	66	(60,40,75) $^\circ$	0.822	0.611	0.083	0.088
MCG+09-20	5.3	76	(40,150,100) $^\circ$	0.789	0.649	0.088	0.100
NGC708	2.7	162	(70,20,130) $^\circ$	0.885	0.695	0.030	0.031
NGC910	3.2	142	(60,70,145) $^\circ$	0.877	0.747	0.078	0.103
NGC1128	2.7	216	(80,130,145) $^\circ$	0.941	0.884	0.015	0.021
NGC1129	4.6	494	(60,10,0) $^\circ$	0.888	0.780	0.047	0.044
NGC1275	3.3	80	(50,140,80) $^\circ$	0.780	0.599	0.087	0.083
NGC2329	1.8	140	(60,50,0) $^\circ$	0.930	0.848	0.034	0.031
NGC2804	1.8	32	(61,132,93) $^\circ$	0.897	0.772	0.068	0.046
NGC3550	6.8	422	(60,20,20) $^\circ$	0.973	0.937	0.028	0.050
NGC3551	0.88	114	(48,48,151) $^\circ$	0.856	0.687	0.090	0.093
NGC4104	1.5	74	(70,130,135) $^\circ$	0.587	0.290	0.083	0.082
NGC4874	1.5	302	(60,30,150) $^\circ$	0.925	0.818	0.025	0.025
NGC6166	2.5	80	(90,47,150) $^\circ$	0.824	0.588	0.082	0.063
NGC6173	1.4	56	(60,120,30) $^\circ$	0.724	0.427	0.088	0.096
NGC6338	2.1	66	(60,60,165) $^\circ$	0.816	0.630	0.055	0.045
NGC7647	3.7	60	(56,53,18) $^\circ$	0.773	0.623	0.033	0.032
NGC7649	3.0	96	(60,130,95) $^\circ$	0.784	0.507	0.081	0.079
NGC7720	1.8	130	(70,60,150) $^\circ$	0.753	0.502	0.076	0.050
NGC7768	2.9	114	(60,40,150) $^\circ$	0.732	0.515	0.098	0.080
SDSSJ0837	2.6	364	(64,136,36) $^\circ$	0.798	0.543	0.101	0.075
UGC716	3.2	130	(40,100,0) $^\circ$	0.817	0.582	0.078	0.081
UGC727	2.6	102	(60,30,170) $^\circ$	0.817	0.638	0.067	0.079
UGC1191	2.5	238	(60,60,40) $^\circ$	0.850	0.691	0.061	0.049
UGC2232	2.2	198	(60,138,62) $^\circ$	0.827	0.717	0.032	0.031
UGC2413	2.2	72	(60,50,130) $^\circ$	0.788	0.538	0.078	0.058
UGC4289	2.3	94	(60,150,60) $^\circ$	0.873	0.770	0.055	0.050
UGC6394	2.9	50	(54,127,102) $^\circ$	0.855	0.689	0.091	0.078
UGC9799	3.0	66	(60,50,145) $^\circ$	0.816	0.667	0.067	0.060
UGC10143	3.3	136	(70,150,165) $^\circ$	0.782	0.569	0.073	0.061
UGC10726	1.7	134	(50,50,80) $^\circ$	0.925	0.867	0.026	0.022
VV161C	3.2	142	(70,50,0) $^\circ$	0.738	0.514	0.066	0.046

Table 3. *Col. 1:* Galaxy name. *Col. 2:* Smallest RMS. *Col. 3:* Number of "good" deprojections. *Col. 4:* The best-fit viewing angles. *Cols 5-6:* Average p and q values. *Cols 7-8:* RMS on average p and q values.

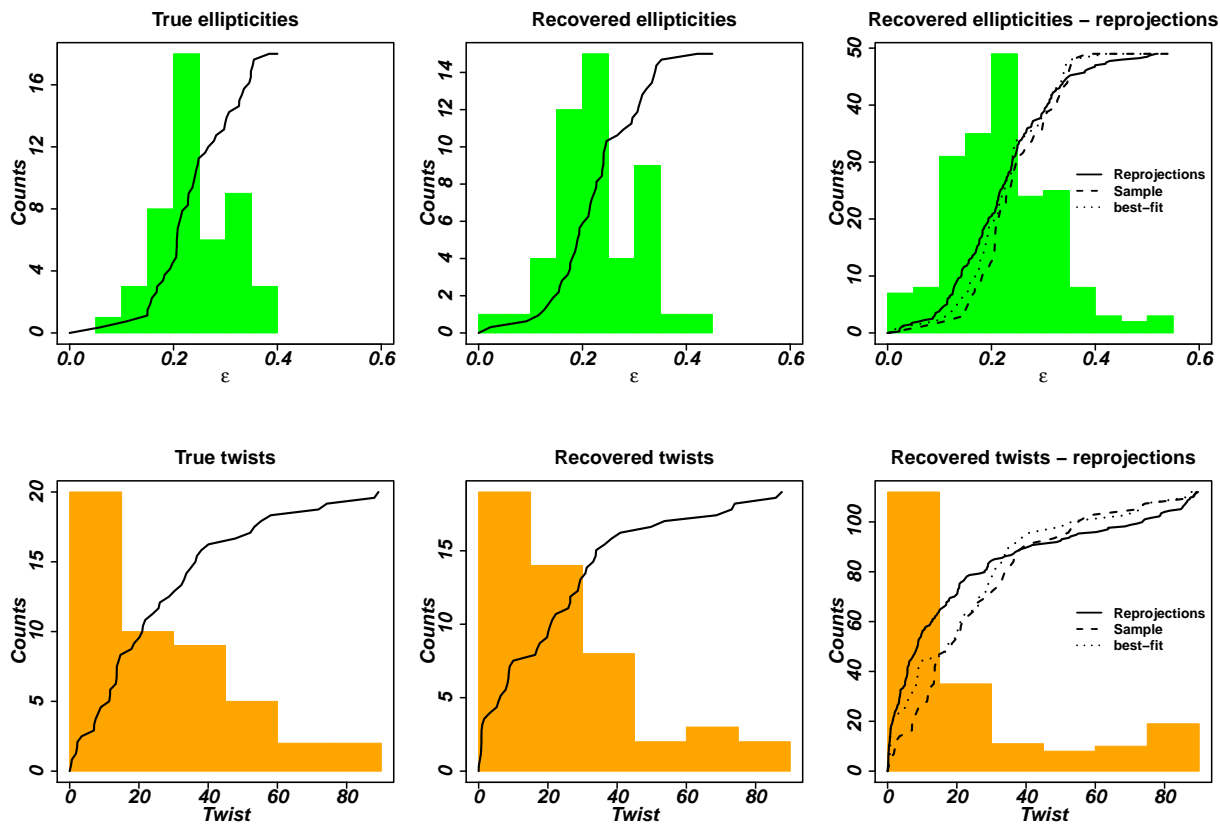


Figure 2. For both ϵ (top row) and PA (bottom row) we present three plots. The left panels show the observed mean values, the central panels the recovered values for the best-fit angles and the right panels the values obtained by re-projecting the best-fit solutions at random viewing angles. The solid lines are the cumulative distribution functions (cdfs), rescaled to the maximum count values. On the right panels we also show the cdf from the left and middle panels by dashed and dotted lines, respectively.

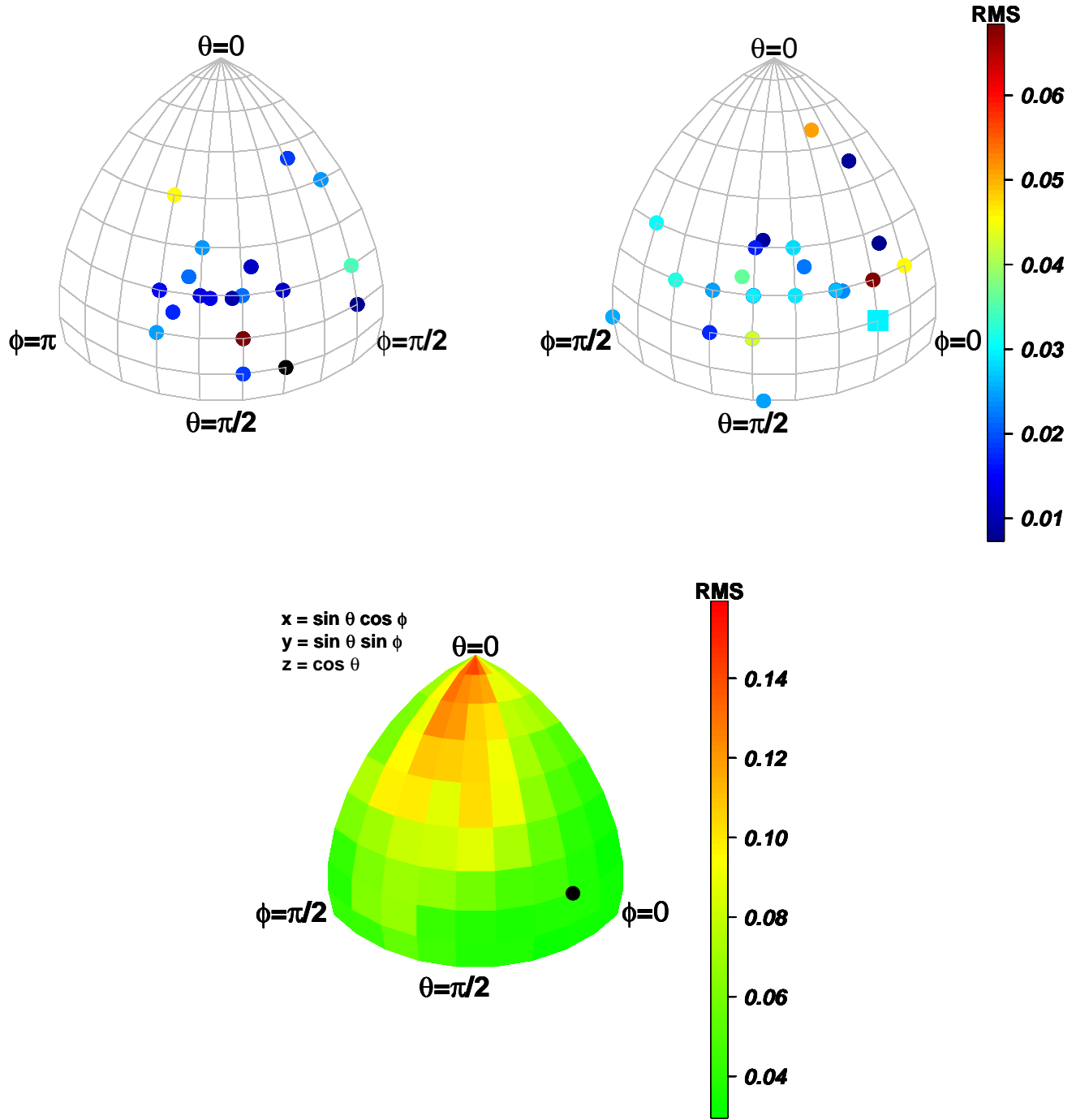


Figure 3. *Top:* Distribution of the best-fit angles on the two octants. The square at $(\theta, \phi) = (70, 20)^\circ$ labels the galaxy NGC708 (see below). The following galaxies appear superimposed: UGC 9799, UGC 2413, MCG-02-02 and NGC 2329 with $(\theta, \phi) = (60, 50)^\circ$; the galaxies MCG+09-13, IC1634, IC 5338 and IC 664 with $(\theta, \phi) = (60, 40)^\circ$; the galaxies 2MASXJ1358 and IC1695 with $(\theta, \phi) = (50, 40)^\circ$; the galaxies LEDA2098, NGC4874 and UGC727 with $(\theta, \phi) = (60, 30)^\circ$; the galaxies LEDA1518 and NGC6338 with $(\theta, \phi) = (60, 60)^\circ$; the galaxies UGC4289 and MCG+03-04 with $(\theta, \phi) = (60, 150)^\circ$; the galaxies MCG+02-04 and NGC 4104 with $(\theta, \phi) = (70, 130)^\circ$. *Bottom:* RMS distribution as a function of (θ, ϕ) for the galaxy NGC708, clearly showing the goodness of solutions close to the principal axes. The black point labels the best-fit solution, located at $(\theta, \phi) = (70, 20)^\circ$.

able deprojections $p(r)$ and $q(r)$ for every galaxy of the sample, i.e. averaged on every "good" deprojection. We get $\langle p(r) \rangle = 0.84$ and $\langle q(r) \rangle = 0.68$, with scatters of ~ 0.1 (see Tab. 3 for the values we get for each BCG). For comparison, Ene et al. (2018) used ellipticity distribution and found $\langle p(r) \rangle = 0.88$ and $\langle q(r) \rangle = 0.65$ for a sample of slow rotators. The histogram of the mean triaxiality parameter, presented in the right panel of Fig. 4, shows that although BCGs follow different scaling relations from ordinary ETGs, they have $0.39 \leq \langle T \rangle \leq 0.72$, in agreement with the findings of Vincent & Ryden (2005) for a sample consisting only of ordinary ETGs. The conclusion here is that the triaxiality is extremely high for every object of the sample, with no object showing a mean triaxiality outside of the $[0.39 - 0.72]$ interval.

We do not detect correlations between $\langle p(r) \rangle$, $\langle q(r) \rangle$ or $\langle T(r) \rangle$ and the size. A weak correlation is seen with absolute magnitudes: bright BCGs appear rounder than fainter ones, having approximately the same triaxiality. The trend is more clearly seen when considering the radial profiles (see Figs. 5 & 6).

4.3. Comparison with the TNG and Magneticum simulations

In order to compare the recovered shape profiles to the shape profiles of simulated galaxies, we use the IllustrisTNG and Magneticum simulations. We consider the 110.7^3 Mpc^3 and 68^3 Mpc^3 cosmological volumes, respectively, as a good compromise between resolution and number of massive galaxies simulated. In TNG100, the mean mass of the stellar particles is $1.4 \times 10^6 M_\odot$ while the dark matter particles have masses $7.5 \times 10^6 M_\odot$. The Plummer equivalent gravitational softening length for both stars and dark matter at redshift $z = 0$ is $r_{\text{soft}} = 0.74 \text{ kpc}$. Instead, Magneticum has stellar particles with masses of $2.6 \times 10^6 M_\odot$ and DM particles with masses of $5.1 \times 10^7 M_\odot$, while $r_{\text{soft}} = 2 \text{ kpc}$ for DM and 1 kpc for stars, respectively.

We select simulated galaxies with total mass larger than $10^{13} M_\odot$ that are the most massive members of their group (so-called 'central'). We divide these galaxies into 2 mass bins, with the number of objects in each mass bin summarized in Tab 4. From these, we derive $p(r)$ and $q(r)$ profiles for the dark matter and the stellar component separately. This is done by diagonalizing the inertia tensor

$$I_{ij} = \frac{\sum_n m_n x_{n,i} x_{n,j}}{\sum_n m_n}, \quad (2)$$

where $x_{n,i}$ are the coordinates of the stellar particles and m_n their mass, calculated in ellipsoidal shells (Zemp

$\Delta \log (M_{\text{tot}}/M_\odot)$	TNG	Magneticum
13-13.35	116	31
≥ 13.35	86	20

Table 4. The number of galaxies for every total mass bin from the TNG100 (second column) and Magneticum (third column) simulations.

et al. 2011). We choose 10 radial bins logarithmically spaced along the intrinsic major axis of the galaxies from 3 to 100 kpc. In each step, the iterative procedure adjusts the flattening of the ellipsoidal shell and the direction of principal axes to the iso-density contours, until it converges within 1% in both p and q . We verified that the variation in the direction of the principal axes are generally within 5 degrees between 3 and 100 kpc and that fixing their position to a mean direction (for example, measured within 1 effective radius) slightly overestimates the axis ratios by a few percent, up to a median $\sim 3\%$ in p and 7% in q at 100 kpc. This allows a comparison with the shape profiles derived for our BCGs with our deprojection code, which keeps the direction of principal axes in the 3D deprojected model fixed.

For each radial bin we compare the average profiles with those derived for our BCGs with our deprojection code, doing the same for the triaxiality parameter $T(r)$. We split the BCG sample into a bright one with $M_{\text{tot}} < -23.7$ and a faint one with $M_{\text{tot}} > -23.7$, each of which with 21 galaxies. Assuming a M/L ratio of 6, this corresponds to a stellar mass of $2.2 \times 10^{12} M_\odot$. Similarly, we split the simulated galaxies in two samples considering a total mass cut of $2.2 \times 10^{13} M_\odot$.

In Figs. 5 and 6 we show the comparison between the average profiles for stars and DM respectively, plotting the BCGs using lines, the simulated TNG100 galaxies using squares and the simulated Magneticum galaxies using triangles. For the BCGs we also show the RMS in each radial bin as error bar, with a typical value of ~ 0.1 . This implies a typical error on the mean value of ~ 0.02 . The RMS for the simulated galaxies is of the same order. The left panels show the faint BCG sample together with the less massive simulated galaxies; the right panels show the bright BCG sample together with the more massive simulated galaxies (see Tab. 4).

Bright BCGs appear slightly rounder than faint BCGs by $\Delta p \sim 0.04$ and $\Delta q \sim 0.08$, but with the same triaxiality. This trend is not obvious when looking at simulated galaxies.

The comparison of the profiles of BCGs and simulated galaxies shows that there is a strong disagreement in

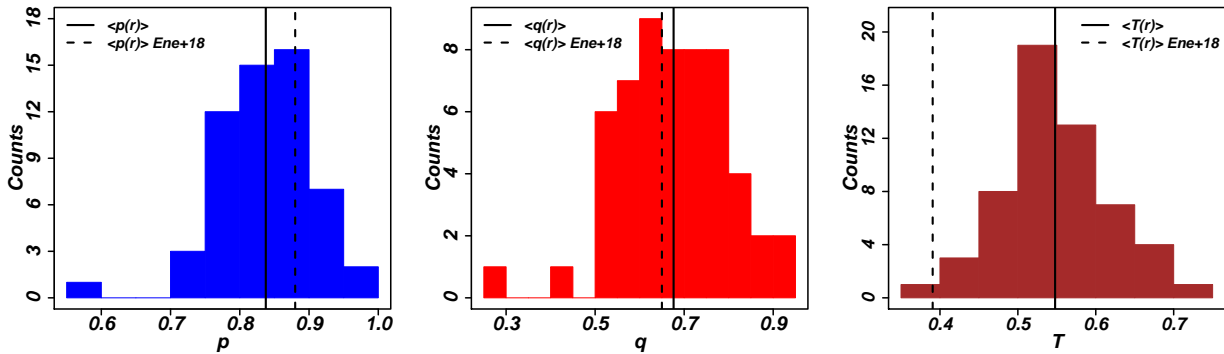


Figure 4. Histograms of the mean intrinsic axis ratios $\langle p(r) \rangle$ (left panel) and $\langle q(r) \rangle$ (middle panel) and of the corresponding triaxiality parameter $\langle T(r) \rangle$ (right panel) for every galaxy of our sample. We also compare the mean values from our histograms with the findings of Ene et al. (2018) from the MASSIVE survey for slow rotators.

the inner regions, especially when the simulated stellar component is considered. The disagreement is less pronounced for the simulated DM halos. In particular, p and q of TNG100 galaxies have values down to 0.2-0.3, which would imply the presence of squashed structures in almost all galaxies. The Magneticum galaxies are generally rounder, but still flatter than the observed ones. This shortcoming of simulations in reproducing the correct distribution of the ellipticity of massive (slowly rotating) systems is well documented: different sets of simulations predict a population of flat slow rotators with ellipticities as high as 0.55-0.6 (Li et al. 2018b using Illustris⁵, Schulze et al. 2018 using Magneticum, Naab & Burkert 2003 using collision-less N -body simulations). In contrast, the observed ellipticity profiles on the sky (see top panels of Fig. 8) demonstrate that most BCGs are round near the center, and it is statistically impossible that all of them are axisymmetric systems viewed close to face-on or pole-on. Turning to the outermost regions, we find a much better agreement between the profiles of BCGs and of simulated galaxies, for both stars and DM. In particular, the BCGs and DM $p(r)$ and $q(r)$ profiles from TNG (and Magneticum at the high-mass end) follow a similar decreasing trend with a slight offset.

The average profile $T(r)$ of our BCGs is almost flat with r at a value of ≈ 0.55 with an RMS scatter of about 0.08, showing that these objects are overall triaxial. The TNG100 simulation generates objects which tend to be prolate in the center and as triaxial as our BCGs in the outer parts. The Magneticum simulation almost matches the observed average profile at intermediate masses when looking at the dark component, but

produces more oblate/prolate profiles in the lower/larger mass bins.

Assuming that the flattening of the stellar component in the simulations compared to the observations is due to implementation in the hydrodynamics scheme and that the dark matter is unaffected by this, the similarity between the observed and simulated DM properties and the fact that the observations show similar triaxiality in the outskirts make it plausible that the light distribution of the outer regions of BCGs is tracing the underlying DM halos and may allow to even probe the nature of dark matter. In particular, recent N -body simulations (Robertson et al. 2019; Fischer et al. 2022) that study mergers of galaxy clusters show that the shape of dark matter subhaloes depends on their physical properties: self-interacting dark matter produces rounder halos than classical λ CDM.

5. CONCLUSIONS

We have deprojected the photometry of a representative sample of 56 BCGs covering a large radial range with good resolution, from the innermost to the outermost regions probing into the intracluster light. The deprojection algorithm is able to generate SB profiles which are representative of the observed photometry. Moreover, the results show that the BCGs are consistent with random orientations in space. For the first time, we have measured radial profiles $p(r)$, $q(r)$ and $T(r)$. The recovered shapes point to strongly triaxial galaxies, rounder at the centre and flatter at large radii. A comparison with the results of the TNG100 and Magneticum simulations shows that BCGs at large radii are a tracer of the DM halo they are embedded in, possibly probing the nature of dark matter. Extending this analysis to galaxies at higher redshifts can probe the formation history of such objects, although getting SB

⁵ For these simulations, values as high as 0.8 are found (Pulsoni et al. 2020).

profiles with high enough signal-to-noise ratio at large values of z certainly represents a challenge for present-day facilities.

The extremely strong triaxiality of these objects stresses the need for triaxial dynamical modeling of the stellar kinematics (e.g. Neureiter et al. 2020) in order to recover unbiased BH mass and M/L estimates, reconstruct the anisotropy profiles of these galaxies and evaluate the effects of the different number of DOF. We will address these issues in two forthcoming papers (de Nicola et. al, in prep.; Neureiter et. al, in prep.).

ACKNOWLEDGEMENTS

We thank the anonymous referee for carefully reading the manuscript and providing us with useful comments which helped us improving the paper. We thank Moritz Fischer for showing us the results of his PhD thesis previous to submission and for interesting discussions.

The Magneticum Pathfinder simulations were partially performed at the Leibniz-Rechenzentrum with CPU time assigned to the Project “pr86re”, supported by the DFG Cluster of Excellence “Origin and Structure of the Universe”. We are especially grateful for the support by M. Petkova through the Computational Center for Particle and Astrophysics (C2PAP).

The LBT is an international collaboration among institutions in the United States, Italy and Germany. LBT Corporation partners are: LBT Beteiligungsgesellschaft, Germany, representing the Max-Planck Society, the Astrophysical Institute Potsdam, and Heidelberg University; The University of Arizona on behalf of the Arizona university system; Istituto Nazionale di Astrofisica, Italy; The Ohio State University, and The Research Corporation, on behalf of The University of Notre Dame, University of Minnesota and University of Virginia.

REFERENCES

- Abell, G. O., Corwin, Harold G., J., & Olowin, R. P. 1989, *ApJS*, 70, 1
- Akaike, H. 1974, *IEEE Transactions on Automatic Control*, 19, 716
- Bender, R., & Möllenhoff, C. 1987, *A&A*, 177, 71
- Bertola, F., & Galletta, G. 1978, *ApJL*, 226, L115
- Chang, Y.-Y., van der Wel, A., Rix, H.-W., et al. 2013, *ApJ*, 773, 149
- Chen, C.-Y., Hwang, C.-Y., & Ko, C.-M. 2016, *The Astrophysical Journal*, 830, 123
- Contini, E., Yi, S. K., & Kang, X. 2018, *MNRAS*, 479, 932
- de Nicola, S., Saglia, R. P., Thomas, J., Dehnen, W., & Bender, R. 2020, *MNRAS*, 496, 3076
- Ene, I., Ma, C.-P., Veale, M., et al. 2018, *MNRAS*, 479, 2810
- Fischer, M. S., Brüggem, M., Schmidt-Hoberg, K., et al. 2022, *MNRAS*, arXiv:2205.02243
- Franx, M., Illingworth, G., & de Zeeuw, T. 1991, *ApJ*, 383, 112
- Genel, S., Nelson, D., Pillepich, A., et al. 2018, *MNRAS*, 474, 3976
- Gerhard, O. 1996, in *Spiral Galaxies in the Near-IR*, ed. D. Minniti & H.-W. Rix, 138
- Goullaud, C. F., Jensen, J. B., Blakeslee, J. P., et al. 2018, *ApJ*, 856, 11
- Hirschmann, M., Dolag, K., Saro, A., et al. 2014, *MNRAS*, 442, 2304

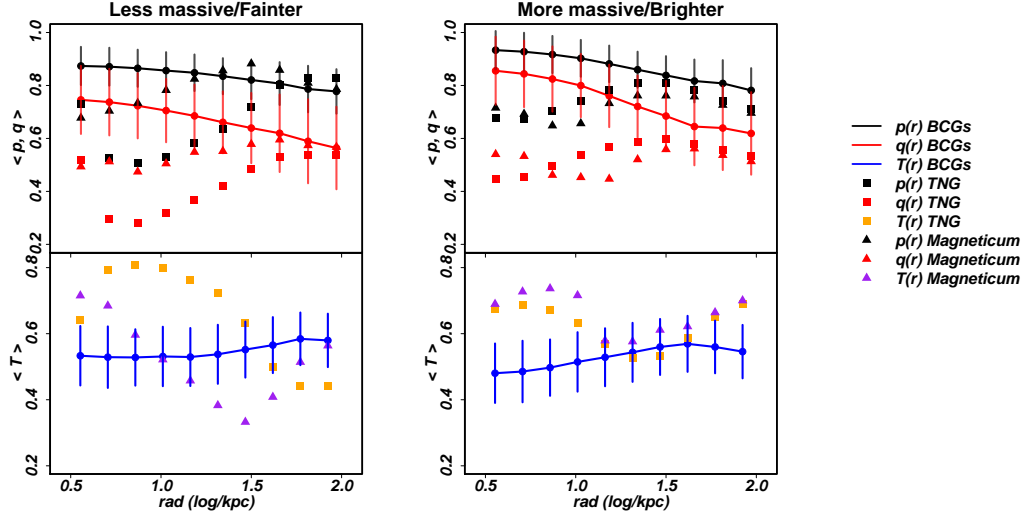


Figure 5. Comparison between the $p(r), q(r)$ average profiles (top panels) and $T(r)$ (bottom panels) of our BCGs and of the stellar component of TNG100 and Magneticum simulations objects. BCGs are rendered using lines, while squares and triangles are used for TNG- and Magneticum-simulated galaxies, respectively. For the BCGs we also compute the RMS in each radial bin, showing it as error bar, with a typical value of $\sim 0.08 - 0.1$.

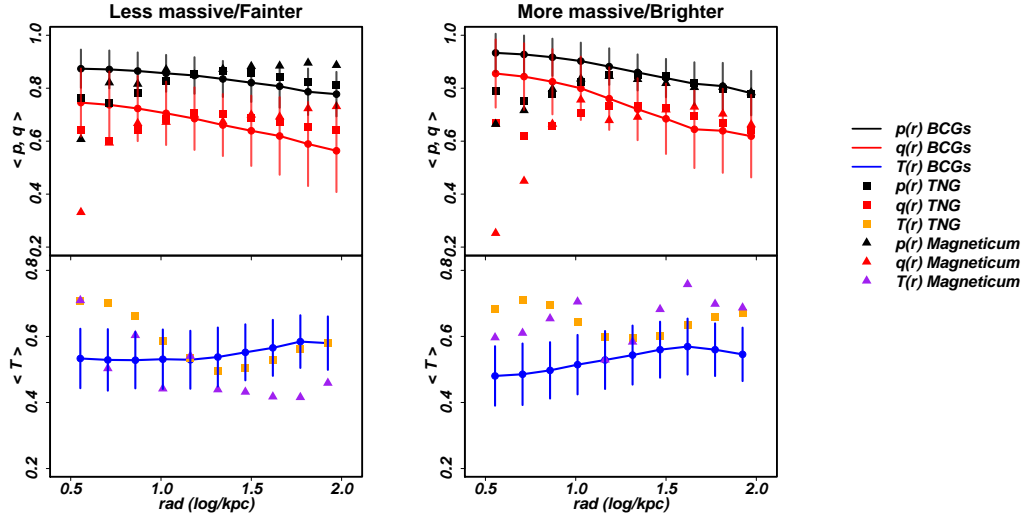


Figure 6. Similar to Fig. 5, but showing the $p(r), q(r)$ and $T(r)$ average profiles of the dark halo component of TNG100 and Magneticum simulations objects.

Illingworth, G., & King, I. R. 1977, ApJL, 218, L109

Kluge, M., Neureiter, B., Riffeser, A., et al. 2020, ApJS, 247, 43

Kolmogorov, A. 1933, Inst. Ital. Attuari, Giorn., 4, 83

Li, H., Mao, S., Cappellari, M., et al. 2018a, ApJL, 863, L19

Li, H., Mao, S., Emsellem, E., et al. 2018b, MNRAS, 473, 1489

Lipka, M., & Thomas, J. 2021, MNRAS, 504, 4599

Marinacci, F., Vogelsberger, M., Pakmor, R., et al. 2018, MNRAS, 480, 5113

Mo, H., Van Den Bosch, F., & White, S. 2008, Galactic dynamics. 2nd ed (Princeton, NJ, Princeton University Press)

Naab, T., & Burkert, A. 2003, ApJ, 597, 893

Naiman, J. P., Pillepich, A., Springel, V., et al. 2018, MNRAS, 477, 1206

Nelson, D., Pillepich, A., Springel, V., et al. 2018, MNRAS, 475, 624

Neureiter, B., Thomas, J., Saglia, R., et al. 2020, MNRAS, 500, 1437

Pillepich, A., Nelson, D., Hernquist, L., et al. 2018, MNRAS, 475, 648

- Pulsoni, C., Gerhard, O., Arnaboldi, M., et al. 2020, *A&A*, 641, A60
- Remus, R.-S., Dolag, K., Naab, T., et al. 2017, *MNRAS*, 464, 3742
- Remus, R.-S., & Forbes, D. A. 2021, arXiv e-prints, arXiv:2101.12216
- Robertson, A., Harvey, D., Massey, R., et al. 2019, *Monthly Notices of the Royal Astronomical Society*, 488, 3646–3662
- Rodriguez-Gomez, V., Snyder, G. F., Lotz, J. M., et al. 2019, *MNRAS*, 483, 4140
- Schulze, F., Remus, R.-S., Dolag, K., et al. 2018, *MNRAS*, 480, 4636
- Smirnov, N. V. 1939, *Bull. Math. Univ. Moscou*, 2, 3
- Springel, V., Pakmor, R., Pillepich, A., et al. 2018, *MNRAS*, 475, 676
- Teklu, A. F., Remus, R.-S., Dolag, K., et al. 2015, *ApJ*, 812, 29
- Teklu, A. F., Remus, R.-S., Dolag, K., & Burkert, A. 2017, *MNRAS*, 472, 4769
- Thomas, J., & Lipka, M. 2022, *MNRAS*, 514, 6203
- Tremblay, B., & Merritt, D. 1996, *AJ*, 111, 2243
- van de Sande, J., Lagos, C. D. P., Welker, C., et al. 2019, *MNRAS*, 484, 869
- van den Bosch, F. C. 1997, *MNRAS*, 287, 543
- Vincent, R. A., & Ryden, B. S. 2005, *ApJ*, 623, 137
- Weijmans, A.-M., de Zeeuw, P. T., Emsellem, E., et al. 2014, *MNRAS*, 444, 3340
- Zemp, M., Gnedin, O. Y., Gnedin, N. Y., & Kravtsov, A. V. 2011, *ApJS*, 197, 30

APPENDIX

A. RESOLUTION AND DEGENERACY EFFECTS

We analyze here the systematic effects stemming from the lack of high-resolution HST or LBT data with Wendelstein observations as well as from the residual degeneracy between the p & q profiles and the viewing angles.

The first point can easily be investigated by deprojecting galaxies with and without high-resolution data, verifying how much the deprojection differs between the two cases. We choose two galaxies, NGC7647 (for the HST case) and UGC10726 (for the LBT case), and re-perform the deprojection using Wendelstein data only for the best-fit viewing angles. These two galaxies represent stringent tests given the very low scatter for both p and q (see Tab. 3) among different solutions at different viewing angles and the code yielding a low best-fit RMS value. Moreover, the central regions of these galaxies are relaxed, meaning that we can exploit HST and LBT data up to the innermost radii.

In the two top panels of Fig. 7 we show the $p(r), q(r)$ profiles from the HST(LBT)+Wendelstein case as solid lines, while the Wendelstein-only profiles are shown as dotted lines for p and q . The Wendelstein-only deprojection cannot probe the inner region of the galaxy, but remains within the region delimited by the RMS (shown as coloured area in the figures) at larger radii.

As a second test, we take the galaxy NGC7647 and deproject it at the best-fit viewing angles (with HST photometry) stopping the deprojection as soon as the RMS reaches $1.5 \times \text{RMS}_{\text{min}}$. In the bottom panel of Fig. 7 we compare this solution to the best-fit one. Also in this case the deviations from the best-fit solution are smaller than the scatter due to the different viewing angles for which an acceptable deprojection is found.

Thus, we conclude the lack of the high-resolution photometry does not change the conclusions reported in this paper. Moreover, considering only the best-fit solution (in terms of the RMS) for a given set of viewing angles probes the range of acceptable p & q profiles.

B. ELLIPTICITY AND PA PROFILES

In Fig. 8 we show the ε and the PA profiles for the BCGs of our sample. Omitted points (see also notes in App. D) are not shown.

C. INTRINSIC SHAPE PROFILES

In Fig. 12 we show intrinsic axis ratio profiles, along with the corresponding triaxiality profiles, for every BCG of the sample. The profiles are computed by averaging over all acceptable deprojections.

D. NOTES ON INDIVIDUAL GALAXIES

- **2MASXJ0753:** This is one of the galaxies observed at LBT. The PSF effects are clearly visible way beyond the $0.4''$ seeing value estimated during the observations, and therefore all the affected points are not taken into account. The galaxy shows bumpy/noisy ε and PA profiles which cannot be described accurately, despite the fact that the viewing angles are not close to the principal axes.
- **2MASXJ0900:** This well-fitted galaxy has a sudden 25° twist in the outermost regions, which is well reproduced. This may be due to the ICL given that in the innermost the regions there is no significant twist.
- **2MASXJ1358:** This is an example of a galaxy whose ε does not change much as a function of the radius. Our best-fit slightly overestimates it, while the twist is underestimated. We stop the deprojection at 75 kpc since the isophotal parameters cannot be adequately fitted anymore beyond this radius.
- **IC613:** The galaxy is very round ($\varepsilon \lesssim 0.1$ until beyond 10 kpc). The outermost radii hint at something not in equilibrium, which the code does fit well. The PA at the centre is not well reproduced, but since ε is small in the central region, this is not a serious issue.
- **IC664:** This is a rare example of a galaxy which is flat in the center and round in the outskirts. This low ε generates an unrealistic twist at large radii, but the galaxy still shows a nice constant PA at lower radii which is well reproduced by the code.

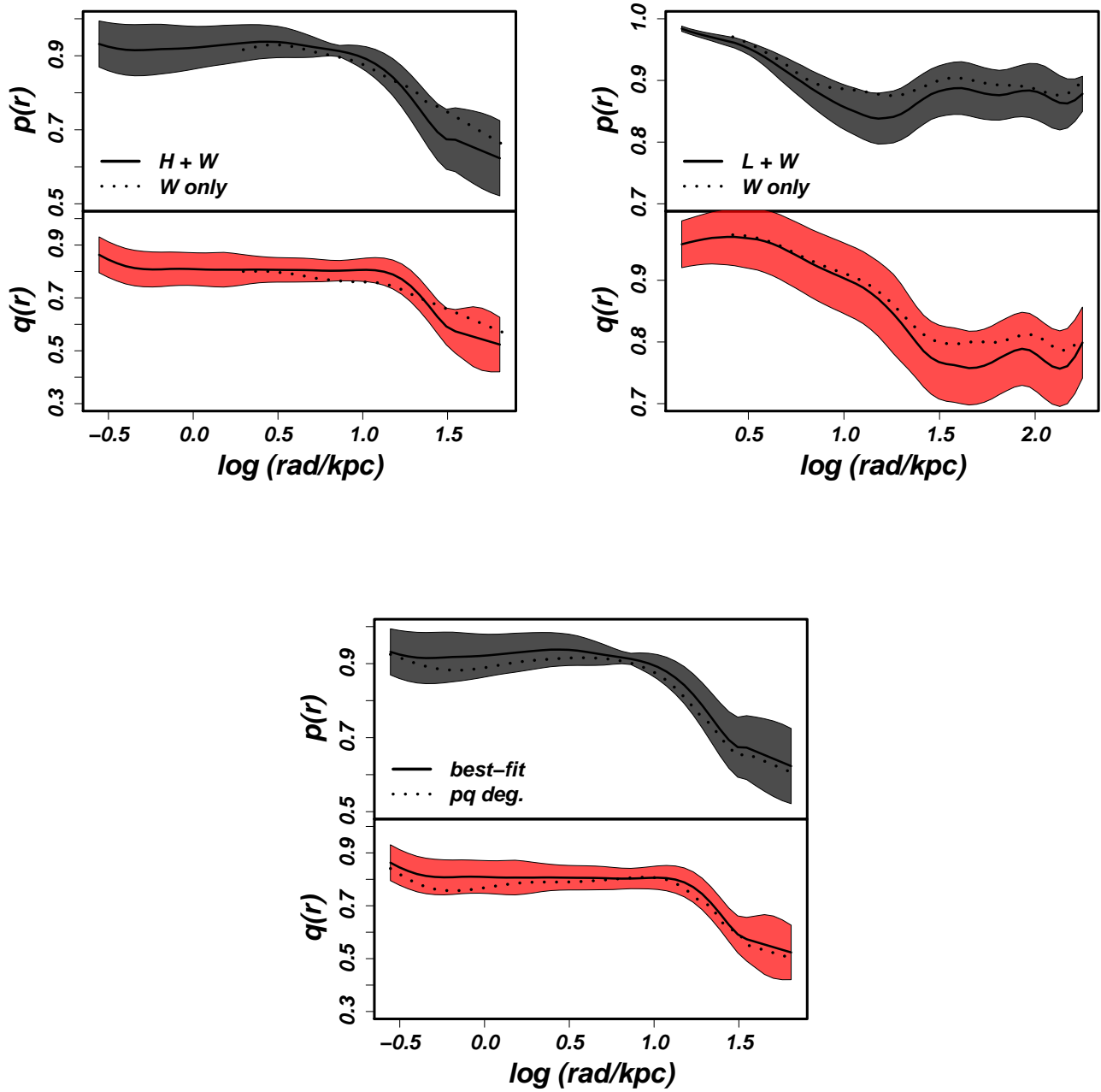


Figure 7. *Top panels:* Comparison of the deprojections obtained at the best-fit viewing angles with or without HST (left, galaxy NGC7647) and LBT photometry (right, galaxy UGC10726). The solid lines are the best-fit profiles with both high-resolution and Wendelstein photometry, while the dotted lines show the solutions with Wendelstein photometry only. The coloured regions are given by the RMS values. *Bottom panel:* For the galaxy NGC7647, we perform a deprojection stopping it when the RMS reaches $1.5 \times \text{RMS}_{\min}$ to judge the effects of possible degeneracies between the model and the viewing angles. The resulting profiles are shown as dotted lines, solid lines and coloured regions are as above.

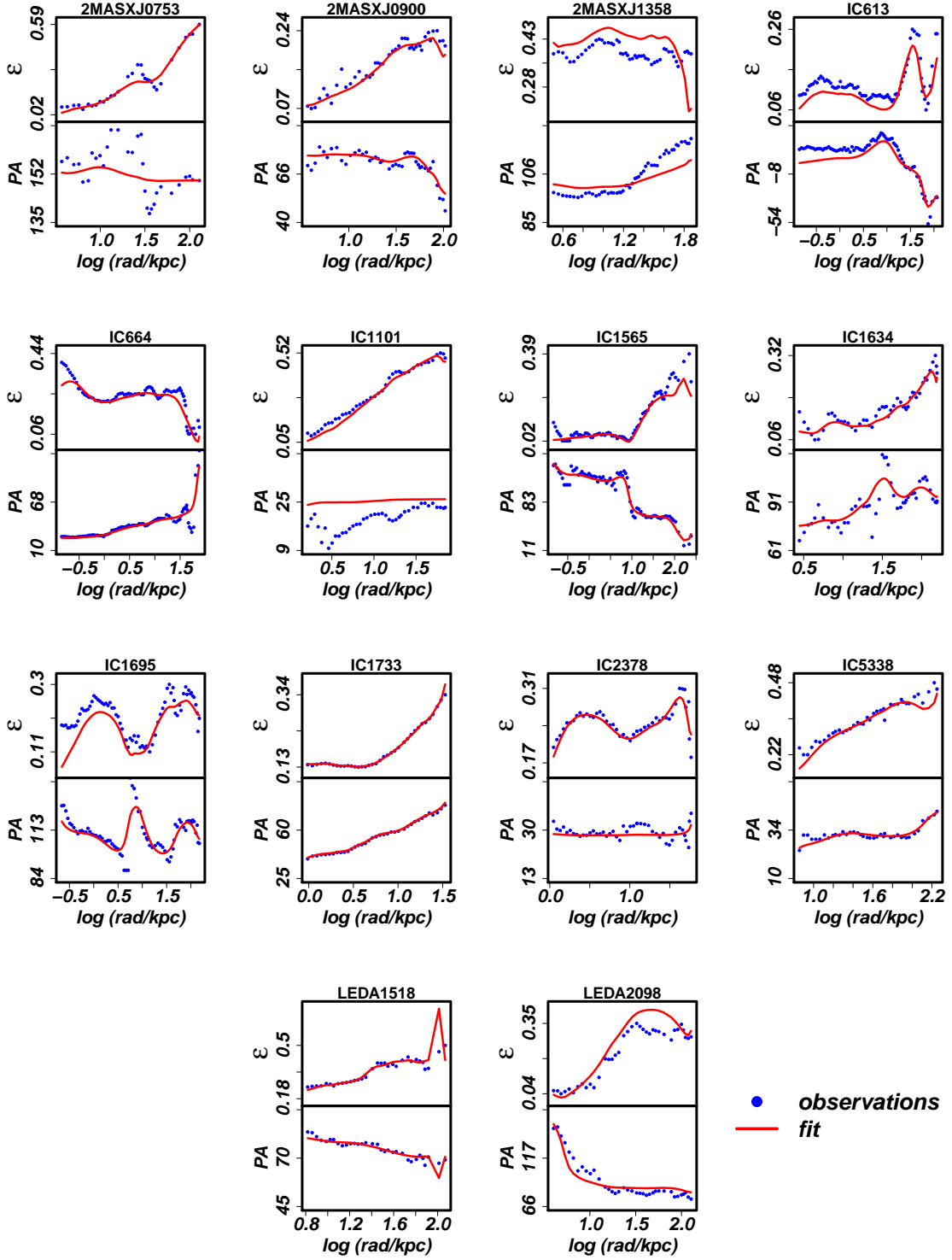


Figure 8. ϵ (top panels) and PA (bottom panels) profiles of every BCG considered in this work. Blue points are the original photometry, whereas the red lines show our fits. The radii are given in \log_{10} kpc.

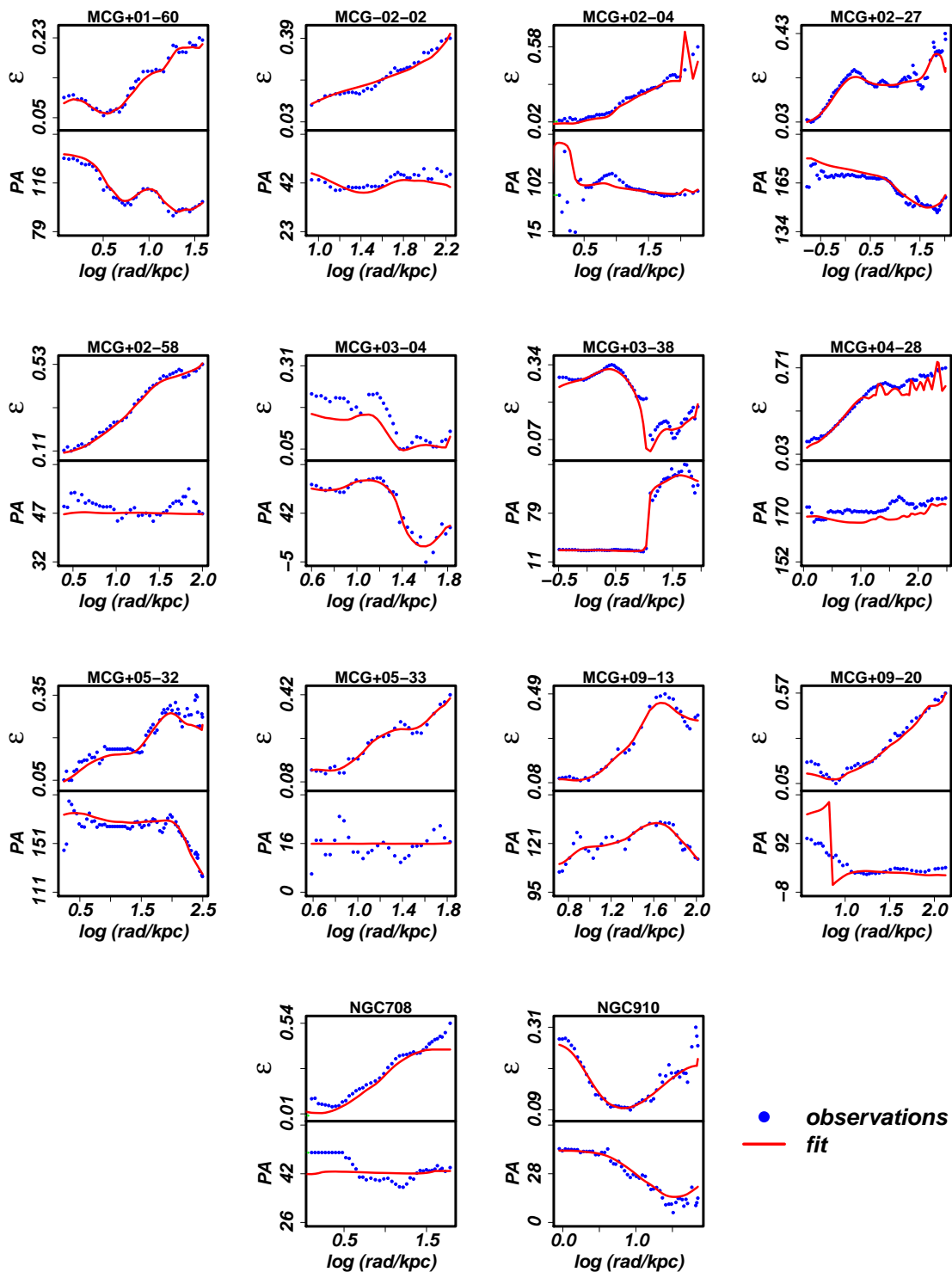


Figure 9. *

Figure 8 (continued)

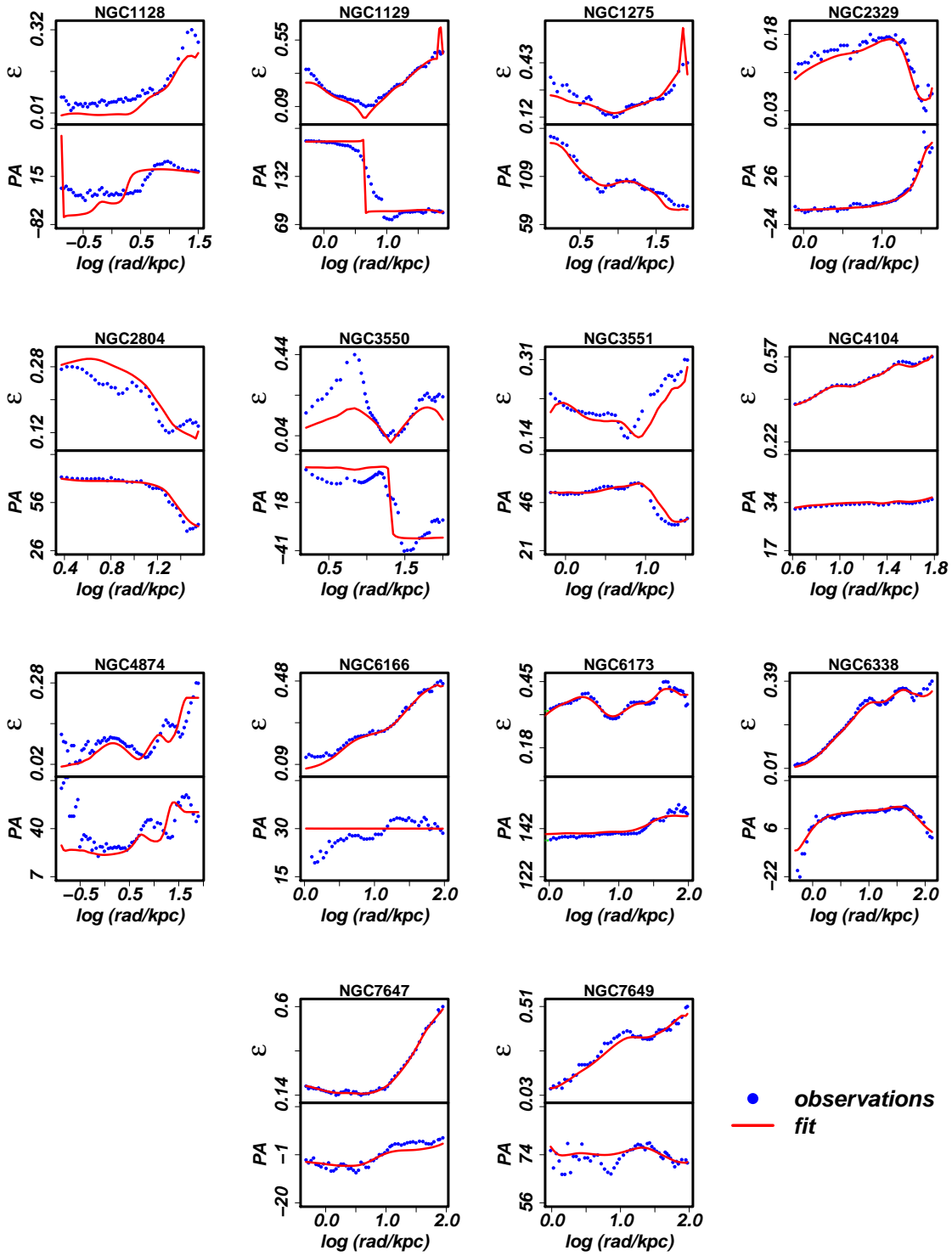


Figure 10. *
Figure 8 (continued)

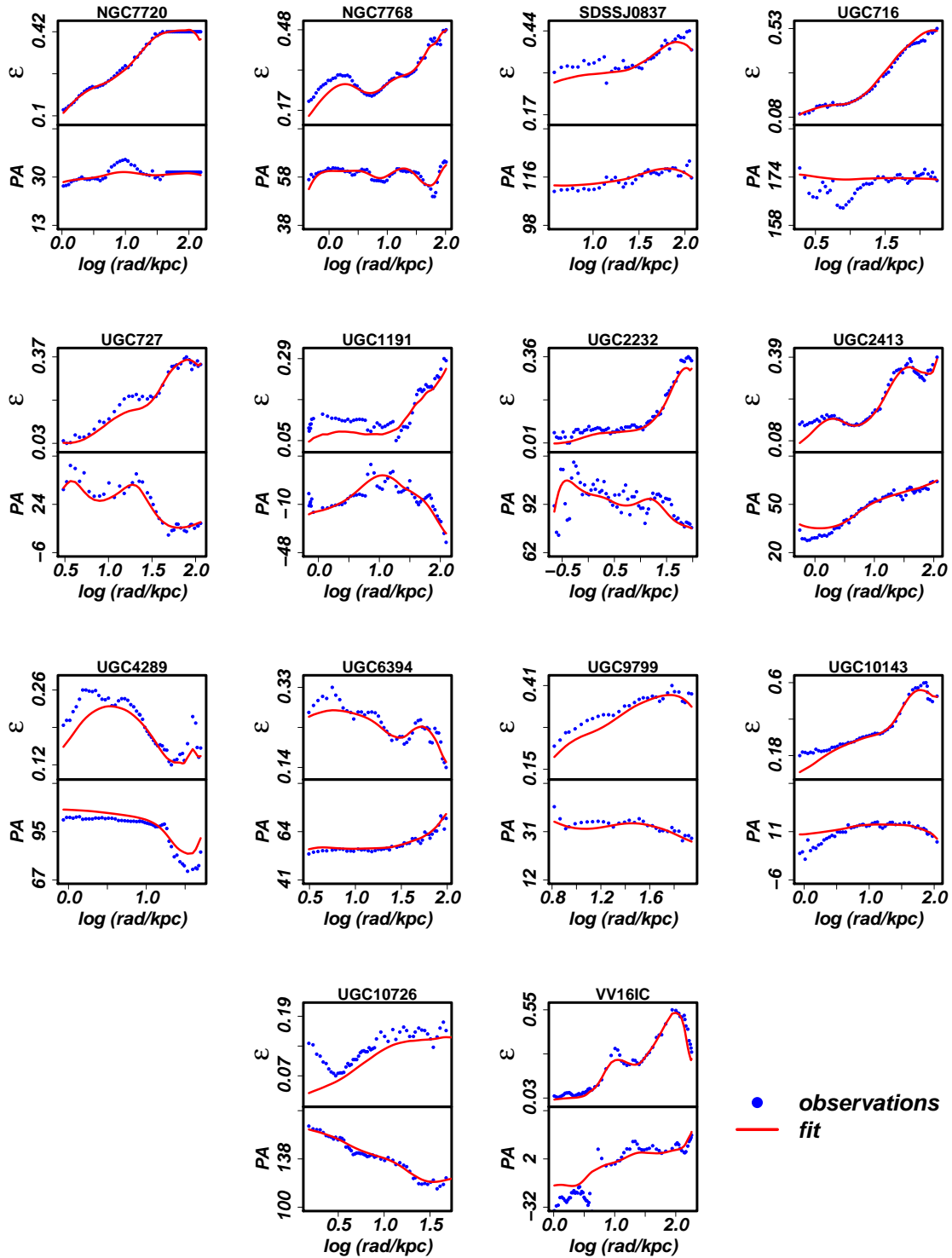


Figure 11. *

Figure 8 (continued)

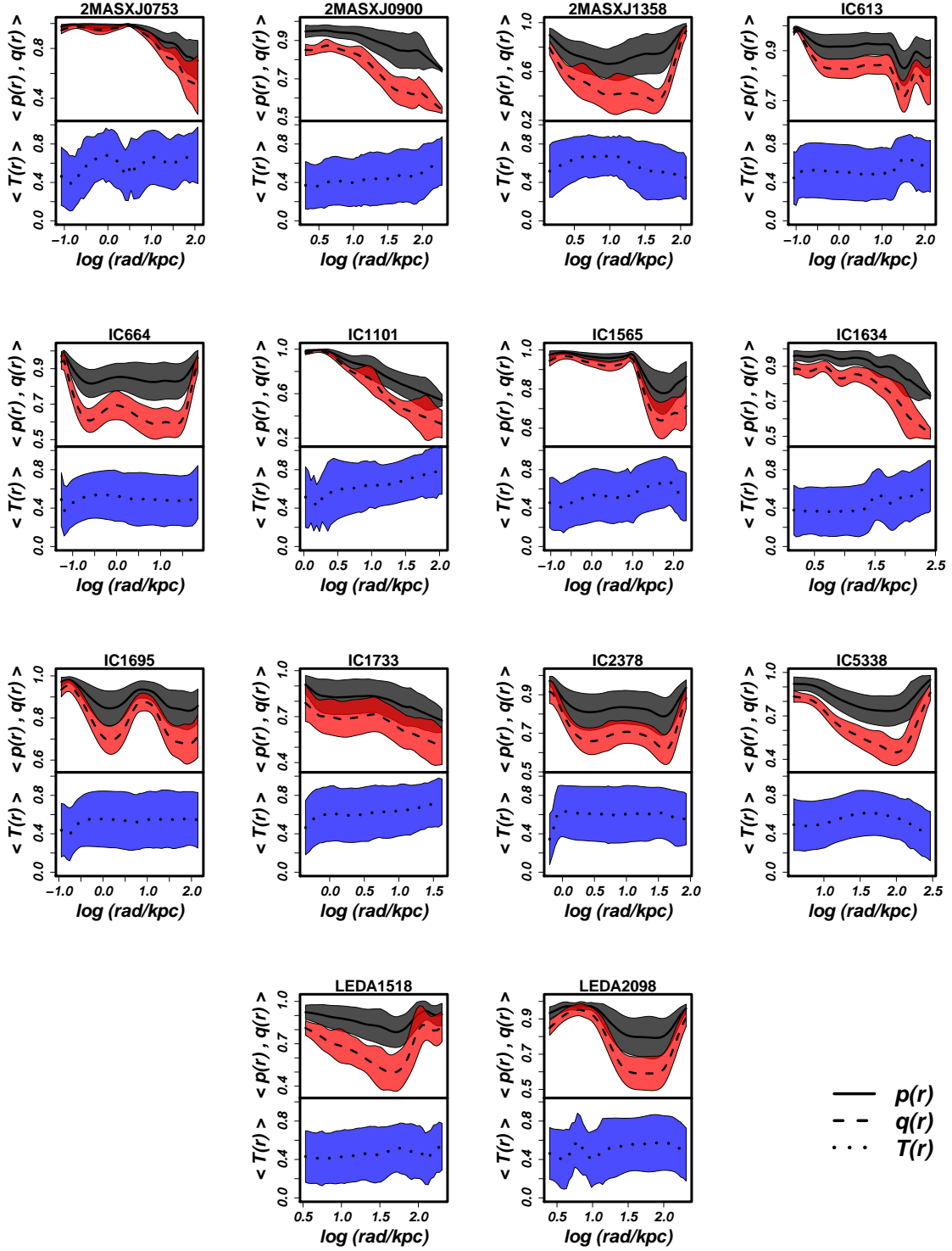


Figure 12. Intrinsic axis ratio p, q (top panels) and triaxiality T (bottom panels) profiles of every BCG considered in this work. The solid, dashed and dotted lines are the average among all good profiles (see Sec. 3.2), while the coloured regions mark the RMS values. The radii are given in \log_{10} kpc.

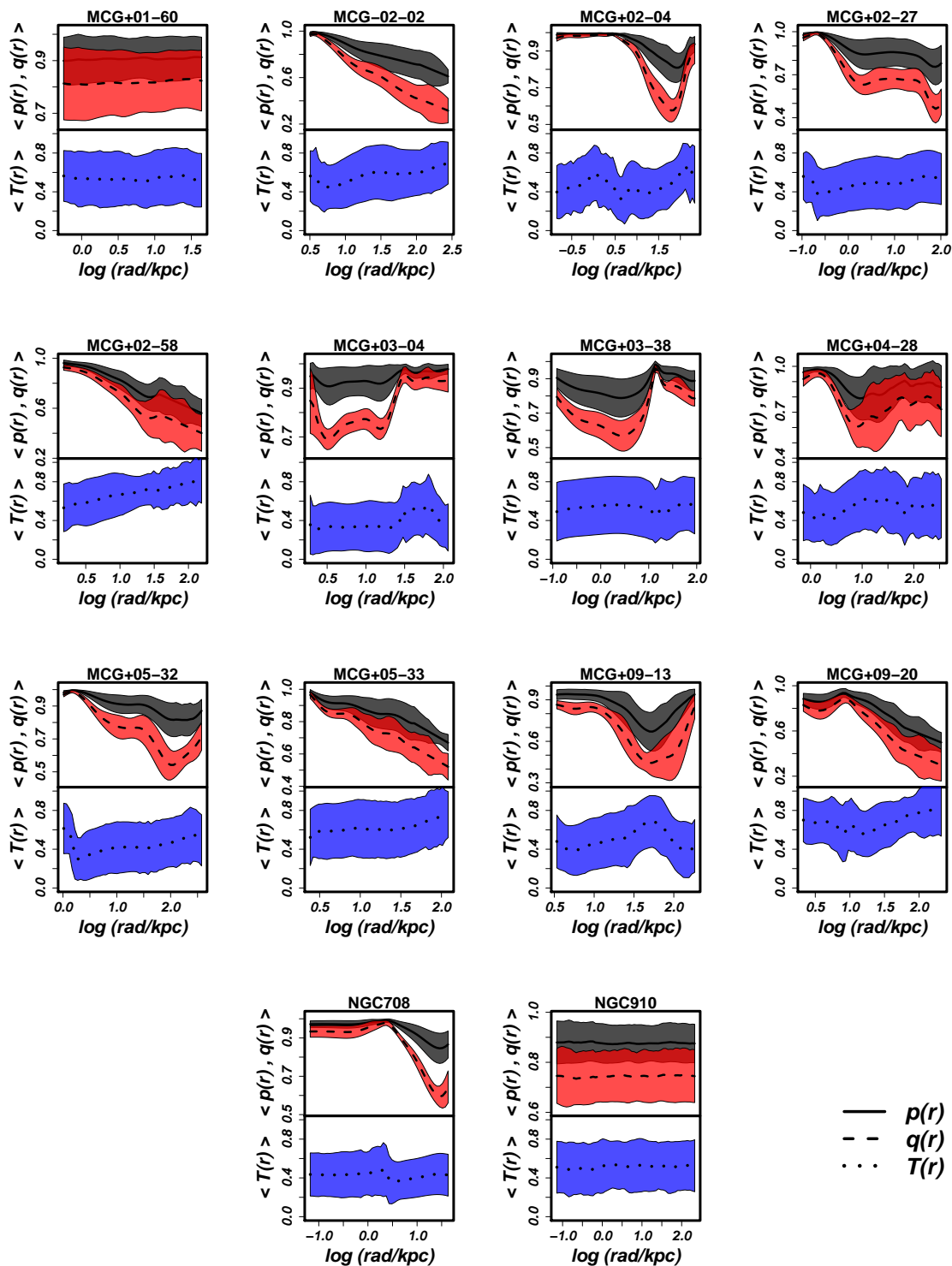


Figure 13. *

Figure 9 (continued)

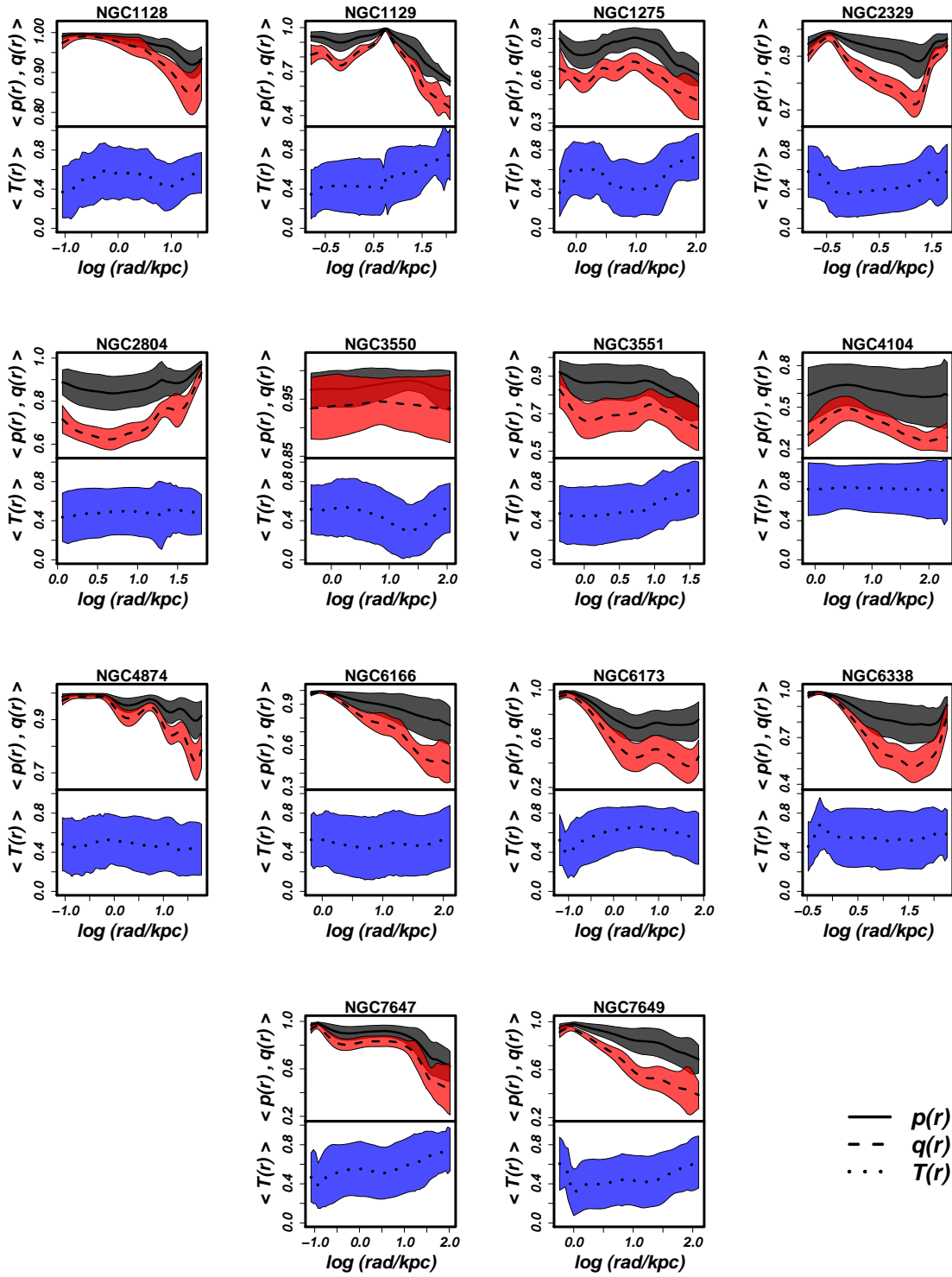


Figure 14. *
Figure 9 (continued)

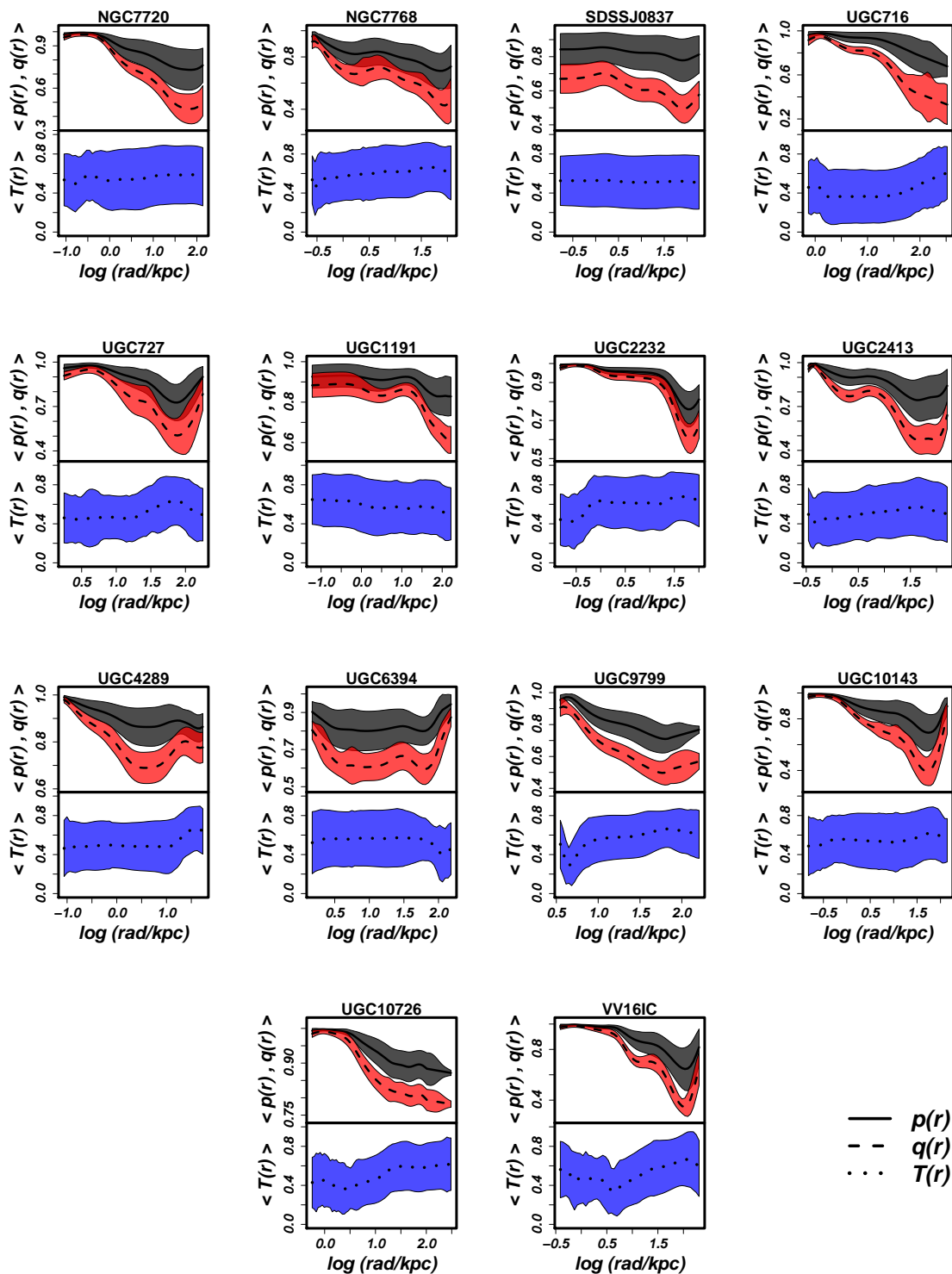


Figure 15. *

Figure 9 (continued)

- **IC1101:** The best-fit angles $(\theta, \phi, \psi) = (50, 80, 160)^\circ$ almost lie on the (y, z) plane, which does not allow for a precise recovery of the twist. Possibly these angles are not the correct ones, because one of the random re-projections does produce a better fit to the observed twist. The somewhat bumpy ε and PA profiles point to the presence of not fully relaxed structures.
- **IC1565:** The galaxy is well fitted with the exception of the outermost ε points which likely belong to the intracluster light. The huge twist shows some oscillations, hinting at a not completely relaxed galaxy.
- **IC1634:** The galaxy has very noisy profiles, which hint at a not yet relaxed galaxy. However, the code reproduces the trends very well.
- **IC1695:** Although both the ε and the PA profiles are complex, the code reproduces these profiles well, with the exception of the major bump in the PA, which is underestimated by a factor of 2.
- **IC1733:** We stop the deprojection at 35 kpc because of possible unrelaxed structures at larger radii. It is the best-fitted galaxy of the sample, with an RMS of 0.0073.
- **IC2378:** The best-fit angles $(\theta, \phi, \psi) = (70, 10, 150)^\circ$ are close to the x -axis. The somewhat noisy but almost constant PA profile allows a good fit with low RMS and indicates that the galaxy might be oriented along one of the principal axes.
- **IC5338:** We start the deprojection at 4.9 kpc because of possible AGN contamination. The last points do give a suspicious twist increase probably linked to the intracluster light; however, this is nicely reproduced.
- **LEDA1518:** The galaxy has a 20° twist and a smooth ellipticity profile, although we note that $\varepsilon > 0.2$ in the central regions already. The deprojection reproduces the profiles very well except for the outermost points.
- **LEDA2098:** The galaxy has a huge 80° twist, but this is mostly given by the very low ellipticity in the central regions. The code reproduces these profiles well, slightly overestimating ε at the outer radii.
- **MCG+01-60:** We start the deprojection at 1.16 kpc, since for this galaxy only Wendelstein data are available. This is another galaxy with $\text{RMS}_{\text{best}} \leq 0.01$.
- **MCG-02-02:** This well relaxed galaxy has a typical ellipticity profile rising steadily and a small 10° twist. No solutions compatible with v.a. along the principal axes are found, but we get acceptable deprojections at $\theta = 10^\circ$.
- **MCG+02-04:** The twist is well reproduced with the exception of a bump around 10 kpc. In the central regions we suspect the galaxy to be not fully relaxed, because of an unrealistic $\sim 150^\circ$ twist at small radii. Therefore, we start the deprojection at 1.3 kpc.
- **MCG+02-27:** The 30° twist present in the central regions is not reproduced very well; however since ε is very low this does not significantly affect the goodness of the fit. The bumpy ε profile suggests that relaxation is not complete.
- **MCG+02-58, MCG+05-33:** The best-fit angles $(\theta, \phi, \psi) = (80, 0, 165)^\circ$ and $(\theta, \phi, \psi) = (60, 10, 130)^\circ$ almost lie along the x -axis and on the (x, z) plane, respectively. This does not allow for a good twist recovery; however, the true PA profiles oscillate around 15° (which would indeed give $\psi = 165^\circ$ if the galaxy were along x) for MCG+05-33 and around 50° for MCG+02-58 (for which $\psi = 130^\circ$ would be the right value). We measure twists oscillating around 20° and 9° , respectively. This indicates that the two galaxies are oriented along one of the principal axes, but possibly not fully relaxed yet.
- **MCG+03-04:** This interesting galaxy is flat in the central regions, where our code slightly underestimates the ellipticity, and gets rounder in the outskirts. The PA profile is tricky, since the twist is small in the central regions before getting significantly bigger at large radii, where ε is small. The fact that the twist is small in the central regions enables the code to obtain good fits close to the principal axes, as for IC2378.
- **MCG+03-38:** Another flat galaxy in the central regions. Both ε and PA jump wildly at ~ 10 -15 kpc, as if a decoupled structure were there in the centre. Nevertheless, the code returns a good fit to the observed photometry.

- **MCG+04-28:** The high RMS (0.122) indicates that the fit is not satisfactory beyond ~ 10 kpc, where the galaxy becomes extremely flat. The somewhat bumpy twist is overall small, therefore the systematic offset between model and data is not worrying.
- **MCG+05-32:** The galaxy is well fitted. The photometry shows an unrealistic twist in the first ~ 10 isophotes, which is probably the result of the low ellipticity.
- **MCG+09-13, MCG+09-20:** These are both galaxies showing typical isophotes of massive ellipticals, although with some bumps. The twist in the central regions for MCG+09-20 is due to ε almost going to 0.
- **NGC708:** Although the best-fit viewing angles are not exactly on the principal axes, there are several good solutions compatible with such inclinations, as shown in Fig. 3. The photometry has not been deprojected within the first 1.2 kpc because of a dust lane. The scale of the plot in Fig. 8 might give the wrong impression of a poorly recovered twist, which is not the case.
- **NGC910:** Like NGC1129, ε goes down and then up again. The 30° twist is well fitted.
- **NGC1128:** We do not include the galaxy in the twist histogram, as ε is almost always below 0.1, except for the outermost radii.
- **NGC1129:** The best-fit angles $(\theta, \phi, \psi) = (60, 10, 0)^\circ$ almost lie on the (x, z) plane. ε goes down to 0 and then increases again. Given that the twist is roughly 90° , this could be a galaxy compatible with viewing angles along the principal axes (as suggested by the best-fit viewing angles) *and* with intersecting p, q profiles.
- **NGC1275:** This peculiar galaxy shows a high ellipticity both in the innermost and in the outermost regions, with a dip in between. The 80° twist is very well recovered.
- **NGC2329:** We omit the innermost points because of an unrealistic bump in ε .
- **NGC2804:** ε decreases towards the outermost regions. In the first 10 kpc, the twist is completely absent. We stop the deprojection at 65 kpc because the isophotal parameters cannot be measured anymore beyond this radius.
- **NGC3550:** This galaxy was observed at LBT under poor seeing conditions. Moreover, both the ε and the PA profiles hint at a not fully relaxed galaxy.
- **NGC3551:** We omit the innermost three isophotes because of resolution problems when deriving the isophotal parameters (only Wendelstein images are available for this galaxy). The deprojection beyond 35 kpc also becomes unfeasible since the galaxy shows signs of non-equilibrium, however the deprojection yields $\text{RMS} \leq 0.01$.
- **NGC4104:** The first $1.5''$ arcseconds must be discarded because of poor seeing. Also the outermost points (from 60 kpc) are omitted due to contamination from a neighbor galaxy. It is one of the flattest galaxies of the sample, with ε always between 0.4-0.6.
- **NGC4874:** Very round galaxy with noisy profiles. We include it in the histogram, although the only region where ε stabilizes above 0.1 is beyond 10 kpc.
- **NGC6166:** The best-fit angles $(\theta, \phi, \psi) = (40, 0, 60)^\circ$ lie on the (x, z) plane. The low RMS might be explained by the fact that with the exception of the innermost radii (where most of the twist occurs but ε is low) the true PA oscillates around the constant PA recovered by the code.
- **NGC6173:** We dropped the poorly fitted central region of the galaxy.
- **NGC6338:** The deprojection starts at $\sim 0.6''$ because of possible AGN activity.
- **NGC7647:** Nothing to signal here.
- **NGC7649, NGC7720, NGC7768:** It is not entirely clear how relaxed the galaxies are. The PA profiles are somewhat noisy with very small twists, while the ε profiles increase smoothly with radius (with the exception of the central regions of NGC7768) with minor dips.

- **SDSSJ0837:** The same considerations about the observations made for 2MASXJ0837 also apply for this galaxy. However, this galaxy does not show signs of non-equilibrium.
- **UGC716:** The best-fit angles $(\theta, \phi, \psi) = (40, 0, 60)^\circ$ almost lie on the (y, z) plane. This is another galaxy which might indeed be close to the principal axes despite the small $\sim 10^\circ$ twist near the round center.
- **UGC727:** See comments of MCG+09-13 and MCG+09-20.
- **UGC1191:** We start the deprojection at ~ 0.6 - 0.7 kpc because of PSF effects. The galaxy has a large twist ($\sim 40^\circ$) which is well reproduced.
- **UGC2232:** Nothing to signal here.
- **UGC2413:** We note a slight offset in the central regions between the true photometry and the recovered one, probably because of resolution effects given by the spherical ρ -grid.
- **UGC4289:** The galaxy shows a somewhat noisy ε profile along with a PA profile with an abrupt $\sim 30^\circ$ twist starting from ~ 20 kpc. We stop the deprojection at 50 kpc because of possible contamination from neighbour galaxies.
- **UGC6394:** The ellipticity decreases as a function of radius and shows some bumps, while the PA profile is much smoother and very well recovered. For this galaxy we also obtain prolate deprojections compatible with the observed photometry.
- **UGC9799:** We start the deprojection at 4 kpc to avoid the center affected by probable AGN contamination.
- **UGC10143:** The same considerations made for UGC2413 also apply to this galaxy. We start the deprojection at 0.6 kpc because of a sudden 100° twist in the innermost regions.
- **UGC10726:** The same considerations made for UGC1191 also apply to this galaxy. We omit the outermost isophotes.
- **VV16IC:** See comments of UGC9799.